Vertical mixing and internal wave energy fluxes in a sill fjord

André Staalstrøm[a,*], Lars Petter Røed[b,c]

[a]Section for Biogeochemistry and Physical Oceanography, Norwegian Institute for Water Research, Oslo, Norway
[b]Research and Development Department, Norwegian Meteorological Institute, Oslo, Norway
Department of Geosciences, University of Oslo, Oslo, Norway

ABSTRACT

We consider the distribution and level of local vertical mixing inside of the Drøbak Sill in the Oslofjord, Norway. The work is motivated by observations of long periods (∼years) of hypoxic or even anoxic conditions in the innermost basin, episodes attributed to weak vertical mixing. In line with earlier work on the subject we assume that the local vertical mixing level inside of the sill is predominantly determined by the loss of energy of propagating, tidally-induced internal waves whose source is the sill region. To investigate possible differences in vertical mixing we estimate the eddy diffusivity in the various basins based on model simulations and observations using three methods whereby the eddy diffusion coefficient is estimated. The model we use is an ultra high-resolution version of the three-dimensional, hydrostatic ocean model ROMS forced solely by barotropic tide well outside of the sill. To evaluate the sensitivity of the model results we perform sensitivity experiments in which the mesh size and various parameters and parameterizations are varied. We find indeed that the internal waves lose most of their energy before they reach the innermost basin, and hence set the scene for long periods of no deep water renewal. The sensitivity experiments reveal that it is important that the model's mesh size is small enough to resolve the dominant wavelengths of the topography. Moreover, we find that the strength of the turbulence production and hence the mixing depends on the initially chosen stratification. The method we use is generic and may be applied to any sill fjord.

© 2016 The Authors. Published by Elsevier B.V. This is an open access article under the CC BY license (http://creativecommons.org/licenses/by/4.0/).

1. Introduction

We consider spatial variations of vertical mixing in a sill fjord in general and the Oslofjord, Norway (Fig. 1) in particular. Our motivation is the impact vertical mixing that has on the ecological environment, specifically observations of frequent anoxic events in the innermost Bunnefjord basin (Figs. 2 and 3). The first to report such events was Beyer and Føyn (1951). Later Gade (1967, 1970) (Fig. 2) found that anoxic events prevailed for long periods (years). As shown by Fig. 3 periods of hypoxic and near anoxic events are still frequent, and underscore, as noted by Gade (1967, 1970), the difference in length of these events in the two basins. As revealed by Figs. 3 and 2 an anoxic and/or hypoxic event ends abruptly and is quickly restored to oxic conditions. The break down is due to deep water renewals occurring when dense and oxygen rich water overflows the shallow sill at Drøbak (Baalsrud et al., 2002; Berge et al.,2010; Dolven et al.,2013). To set the scene for another deep water

renewal vertical mixing has to reduce the density of the deep water. Thus a low vertical mixing tend to admit hypoxic or even anoxic events to develop for extended periods. The more modern and recent observations depicted in Fig. 3 therefore supports the suggestion made by Gade (1967, 1970) that the difference in vertical mixing level in the Bunnefjord basin and the Vestfjord basin explains the difference in the lengths of the hypoxic and/or anoxic events.

The question arising is why there is a difference in the vertical mixing level. From the literature it is well known that when tides are forced across sills or across submarine ridges internal waves are generated and propagate for long distances before they eventually break and causes mixing (Alford, 2003; Baines, 1982; Egbert and Ray, 2000; Inall, 2009; Ledwell et al., 2000; Sjöberg and Stigebrandt, 1992; St. Laurent and Garrett, 2002; Staalstrøm et al., 2012; Stigebrandt, 1976,1979; Wunsch and Ferrari, 2004; Xing and Davies, 2011). Our hypothesis is therefore that the level of vertical mixing at any location in the Oslofjord inside of the Drøbak Sill critically depends on how much energy is made available via breaking of propagating, tidally-induced internal waves whose source region is the sill. This

* Corresponding author at: Gaustadalleen 21, 0349 Oslo, Norway.
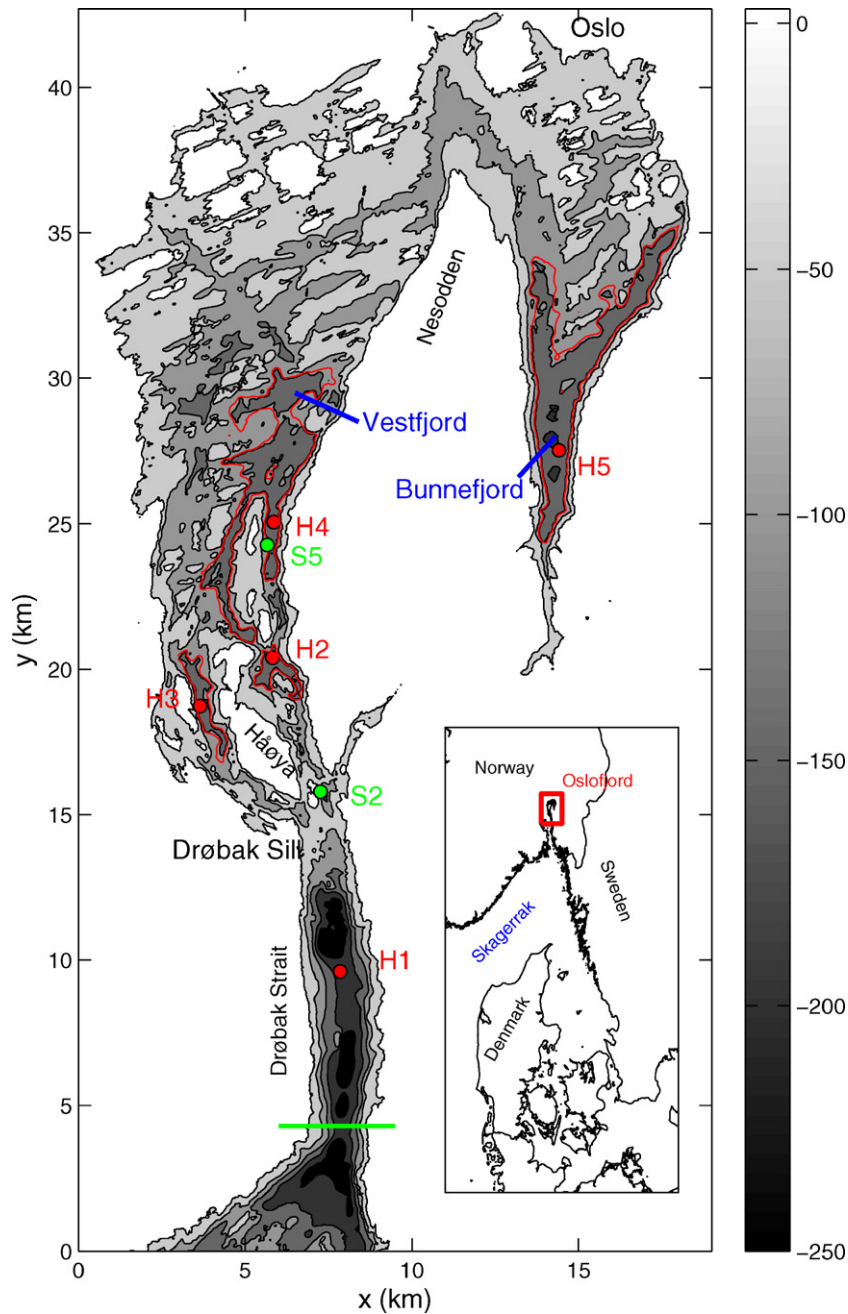 *E-mail address:* ans@niva.no (A. Staalstrøm).

Fig. 1. Map of the Inner Oslofjord. Depth contours are drawn for every 50 m. The green horizontal line at the bottom of the graph marks the southern open boundary of the model. Moorings were deployed at Stations S2 and S5 in 2009 (marked with green circles). Stations H1, H2, H3, H4 and H5 marked with red circles are standard hydrographic stations from the monitoring program. Four different basins are separated by the 90 m depth contour (red line). The maximum depth in the model area is 258 m (in the Drøbak Strait south of the Drøbak Sill) and the shallowest depth is 20 m which is the Drøbak Sill.

hypothesis is not new, but was suggested already by Stigebrandt (1976, 1979). We emphasize though that we do not assume a priori that all the energy is lost before the internal waves reach the innermost Bunnefjord Basin. Rather, by combining results from numerical model experiments and observations, we investigate the geographical distribution of where energy is lost inside of the Drøbak Sill. Thus we are able to possibly answer the question posed at the beginning of the paragraph. We focus on the part of the energy budget in the fjord concerning deep water mixing and energy fluxes due to internal waves. The conversion from barotropic to baroclinic energy, and the relation between energy in internal waves and local dissipation have been studied in the Oslofjord by Staalstrøm et al. (2012,2015).

Specifically we analyze results from a series of tidally forced only simulations of the Oslofjord using the Regional Ocean Modeling System — ROMS (Haidvogel et al.,2008; Shchepetkin and McWilliams, 2005) without actually resolving the processes responsible for the transfer of energy from the mean to the turbulent motion in detail. We emphasize that all the details of the vertical mixing processes are not yet fully understood, and hence they are in general difficult to parameterize correctly (e.g., Berntsen et al., 2009). Finally we note that the model we use features terrain-following vertical coordinates. Hence it is exposed to the well known pressure gradient error (PGE) (Haney, 1991). The PGE is minimized by constructing a special vertical transform that differs from those available in the canonical ROMS. Details on the latter is given in the Appendix.
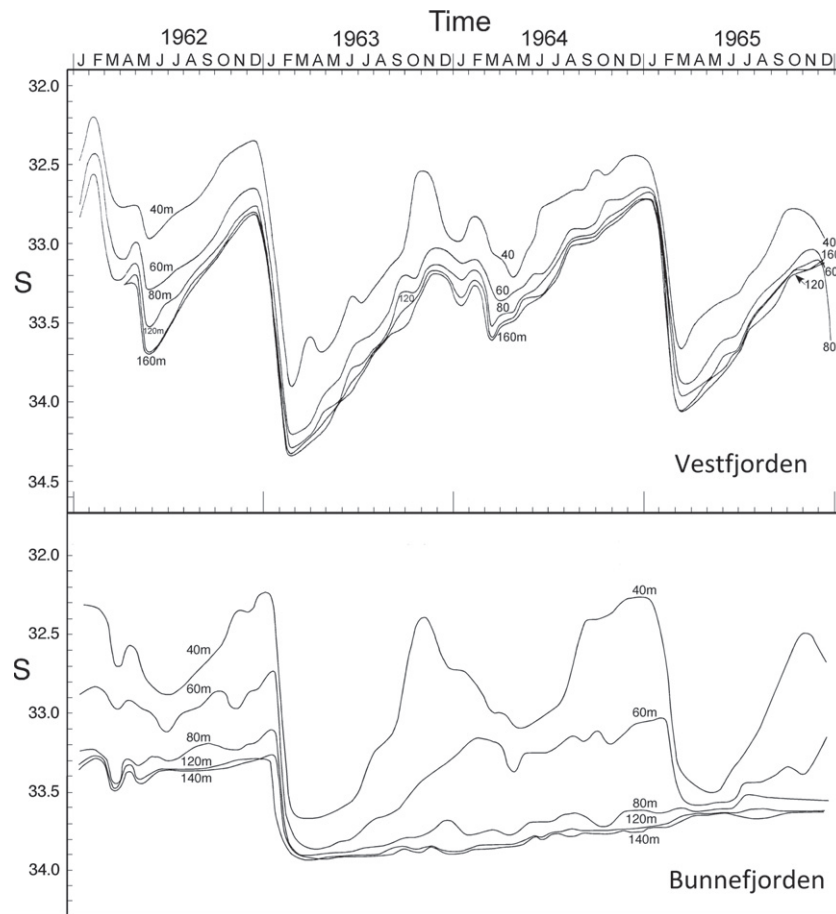
Fig. 2. Salinity at different depths in the Vestfjord (upper panel) and in the Bunnefjord (lower panel). Figure is taken from Gade (1967). Figure is taken from Gade (1967). (Courtesy of NIVA.)

The paper is organized as follows. In Section 2 we give some insight into the characteristics of the inner Oslofjord, while the three methods we use to estimate the spatially varying vertical mixing or eddy diffusion coefficient are outlined in Section 3. In Section 4 we describe the configuration of the MAIN experiment and evaluate the model's performance against observations. Next (Section 5) we examine the results in terms of the internal wave energy flux, turbulence production and the eddy diffusion coefficient. This is followed by Section 6 in which we discuss the sensitivity of the results in terms of the eddy diffusion coefficient by varying some of the key parameters such as the irregular coastal geometry and topography, resolution, stratification and turbulence closure scheme. Finally Section 7 offers a summary and some concluding remarks.

2. The Oslofjord

We focus on the part of the Oslofjord, inside of the Drøbak Sill (Fig. 1). The maximum depth in the model area is 258 m (in the Drøbak Strait south of the Drøbak Sill) and the shallowest depth is 20 m which is the Drøbak Sill. The sill is partly man made and partly natural. The man made part is an underwater barrier called the Drøbak Jetty (Fig. 4). The depth of the jetty is only 1–2 m. There are two narrow openings in the Jetty with a maximum depth of about 6 m. One is located close to the mainland on the western side, while the second runs east–west and is located midway just south of Kaholmen. The remaining eastern part of the sill is natural with a maximum sill depth of slightly less than 20 m. Furthermore, the Håøya divides the entrance to the inner Oslofjord proper into a

western and eastern channel (Fig. 4). The man made jetty effectively hinders the exchange of water via the western channel. Hence most of the exchange of water is via the eastern channel.

In the eastern channel there are two major secondary sills (Fig. 5). They are located 1.5 (47 m deep) and 3.3 km (62 m deep) inside of the main sill. In addition there are several secondary sills north of them. Further into the fjord there are four deeper basins and several shallower ones. The deeper ones all have depths well beyond 90 m. The Vestfjord basin and the Bunnefjord basin both feature maximum depths of about 150 m and are separated by a major sill (Fig. 5) where the fjord makes an almost 180° bend into the Bunnefjord basin.

Several measurement campaigns have been undertaken in the Oslofjord. In 1973 a monitoring program with regular measurements of hydrography and oxygen was undertaken (Baalsrud et al., 2002; Berge et al., 2010). The program features the five stations H1 through H5 in addition to S2 and S5 (Figs. 1 and 4). Special measurements of temperature, conductivity and currents at several depths were recently conducted (2009) in the area in addition to moorings deployed for a month at Stations S2 and S5 as reported by Staalstrøm et al. (2012).

These special measurements are used here to estimate internal wave energy fluxes for comparison with the model results, while the earlier data, e.g., from the monitoring program is used to estimate the turbulent diffusivity using the budget method (cf. Section 3.3). Based on measurements at these sites Staalstrøm et al. (2012) estimated that the vertical mixing below 90 m is at least five times higher at Station H2 compared to the other stations further away
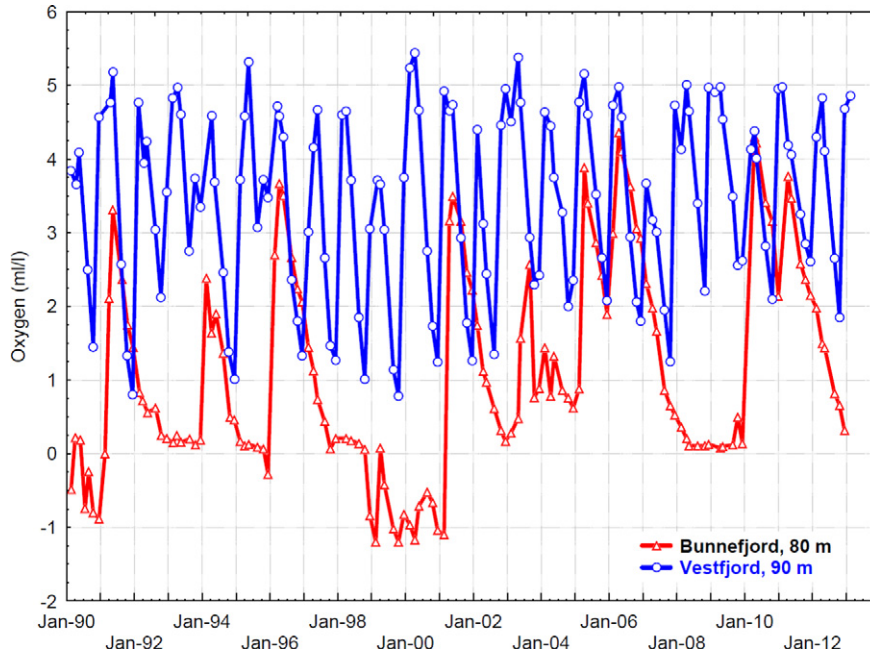
Fig. 3. Time series of oxygen content in ml/l in the Bunnefjord (red curve) and the Vestfjord (blue curve) for the period January 1990 through December 2014. Note the long periods of anoxic (zero or negative oxygen values) and hypoxic (values lower than 2ml/l oxygen content) events in the Bunnefjord compared to the short period of hypoxic events in the Vestfjord.
(Courtesy of Jan Magnusson and Anna Birgitta Ledang, NIVA.)

from the sill. If, as we propose, the energy for the vertical mixing is through breaking, propagating tidally-induced, internal waves, we should experience a marked decrease in the internal wave energy flux as the wave proceed into the fjord.

3. Analyses methods

In the Oslofjord, as in most sill fjords, propagating, tidally-induced internal waves, whose source region is the sill, dominates the dynamics inside of the sill (Gade, 1970; Stigebrandt, 1976, 1979).

We may therefore safely assume that internal wave breaking is the most likely source for local interior vertical mixing. Let w'' and ρ'' be the turbulent components of the vertical velocity and density generated by the breaking internal waves. We may then link these turbulent components to the local vertical eddy diffusion coefficient K by using the common down-the-gradient parameterization of the eddy diffusive flux. Hence

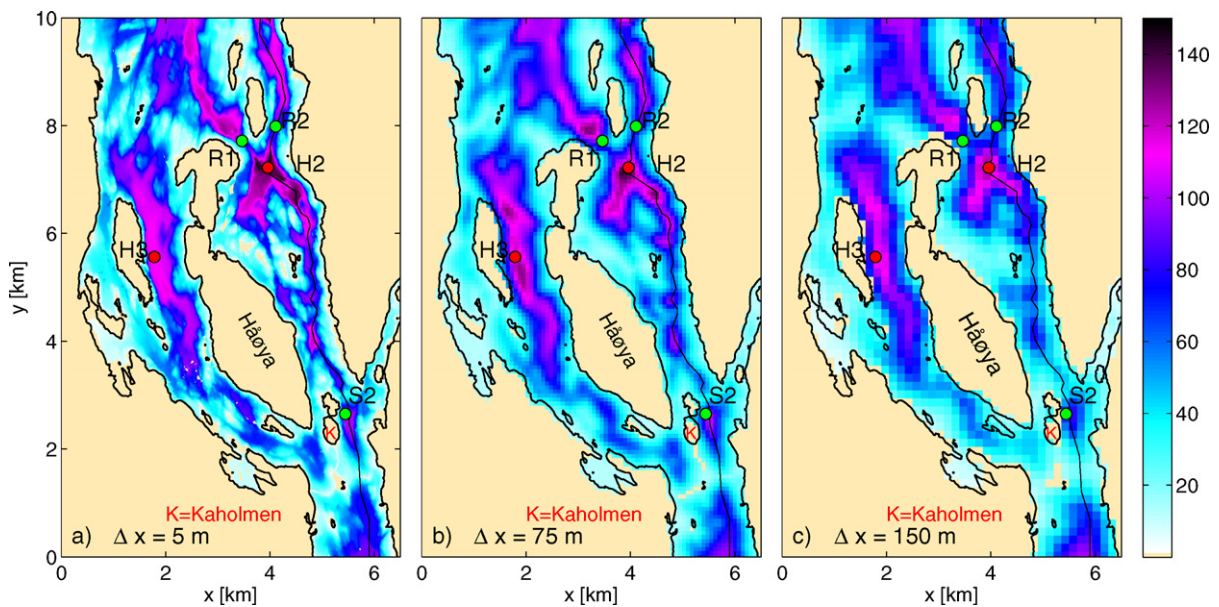$$\overline{w''\rho''} = -K\partial_z\overline{\rho}, \tag{1}$$

Fig. 4. Comparison of observed and model bathymetry in the sill area. a) Observed bathymetry with 5 m grid resolution (Lepland et al., 2009) . b) Model bathymetry with 75 m grid resolution, and c) model bathymetry with 150 m grid resolution. The positions of Stations S2, R1 and R2 are marked with green circles and Stations H2 and H3 with red circles. All depth maps have the same depth scale in metres as given by the color bar to the right.
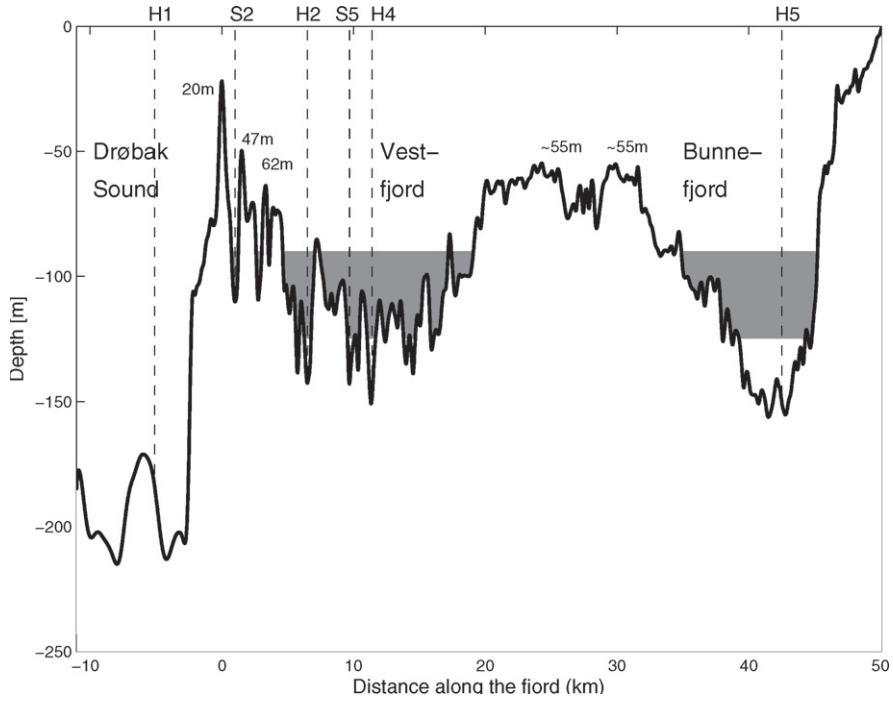
Fig. 5. Depth profile along the fjord following the deepest parts from the Drøbak Sound, on the east side of the Håøya to the inner parts of the Bunnefjord. Vertical dashed lines indicate the positions of the stations along this line. The most important sills—the Drøbak Sill (20 m), the Godthol Sill (47 m), the Tronstad Sill (62 m) and the two sills between the Vestfjord and the Bunnefjord (55 m)—are marked with numbers (Staalstrøm et al., 2012). The gray shaded areas indicate the depth range 90 to 125 m.

where $\bar{\rho}$ is the mean density and the overline notation denotes the Reynolds average. Our focus is on estimating K. To this end we use three methods, namely, the indirect, the direct and the budget methods.

3.1. The indirect method

This method is based on the turbulent kinetic energy equation (TKE). Following Osborn (1980) and others (e.g., Gregg, 1987; Nash et al., 2005; Peters and Bokhorst, 2001) we get

$$K = \frac{T_P - \epsilon}{N^2} = \frac{R_f T_p}{N^2}. \tag{2}$$

Here ϵ is the dissipation of TKE, $N^2 = -g\partial_z\hat{\rho}/\hat{\rho}$ is the Brunt–Väisälä frequency, g being the gravitational acceleration, R_f is the so called mixing efficiency[1] and T_P is the turbulence production defined by

$$T_P = -\frac{1}{\rho_0}\nabla \cdot \mathbf{e}_F, \tag{3}$$

where $\mathbf{e}_F$ is the internal, or baroclinic, wave energy density flux and ρ_0 is a reference density. As revealed by the second equality in Eq. (2) there is a linear relationship between the turbulence production and the eddy diffusion coefficient. Hence a high turbulence production leads to high mixing and vice versa provided R_f and N^2 are fairly constants. Rather than estimating these variables at a single point we opt to estimate them as basin averages. Let the coordinate directed into the fjord be denoted by y (Fig. 6), then a basin volume V is bounded by the fjord walls and two open cross section located say at y_1 and

y_2, respectively. The turbulence production per unit volume within V is then

$$T_P^V = \frac{1}{V}\int_V T_P dV = -\frac{1}{\rho_0 V}\int_\Omega \mathbf{e}_F \cdot \mathbf{n}d\sigma, \tag{4}$$

where $\mathbf{n}$ is the outward normal vector to the surface Ω encompassing the volume V. Assuming that there is no flux through the walls the net turbulence production due to breaking of internal waves in the basin is

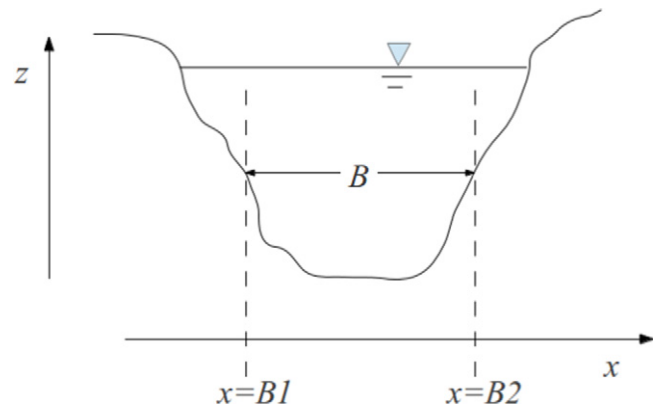$$T_P^V = \frac{F(y_1) - F(y_2)}{\rho_0 V}. \tag{5}$$

Fig. 6. Sketch showing a cross section of the fjord. Note that the width B is a function of of the along fjord coordinate y as well as the depth z.

---

[1] $R_f = B_F/T_P$ where $B_F = N^2 K$ is the buoyancy flux. Thus $R_f \in [0, 1]$. If $R_f = 0$ all the turbulence production is dissipated. If $R_f = 1$ all the turbulence production is used for mixing.

where

$$F(y) = \int_{-H}^{0} \left(\int_{B_1(y, z)}^{B_2(y, z)} \mathbf{e}_F \cdot \mathbf{j} dx \right) dz \qquad (6)$$

is the internal wave energy flux through a cross-section located at y. Here B_1 and B_2 denote the cross-sectional position of the two fjord walls so that $B = B_2 - B_1$ is the width of the cross section at any depth z at location y. If Eq. (5) is positive then energy is lost and turbulence is produced in the basin.

To estimate the flux $F(y)$ we closely follow the method outlined by Nash et al. (2005). Accordingly we estimate the tidally-induced, internal wave energy flux by the pressure work only, that is, $\mathbf{e}_F = p'\hat{\mathbf{u}}'$, where p' and $\mathbf{u}'$ are respectively the pressure and velocity perturbations due by the internal wave motions and the wide-hat notation denotes an average over at least two dominant tidal periods. Possible contributions from advection, diffusion and non-hydrostatic effects are therefore neglected (Kang and Fringer, 2012). This is justified since we perform a basin volume average and consider basins bounded by cross-sections sufficiently far away from where the major diffusion and dissipation takes place. With our choice of coordinate system we therefore get

$$F(y) = \int_{-H}^{0} \left(\int_{B_1}^{B_2} \widehat{p'v'} dx \right) dz, \qquad (7)$$

where p' and v' are computed from

$$p' = p_s - \int_z^0 g\rho'(z)dz \quad \text{and} \quad v' = v - \frac{1}{H}\int_{-H}^0 vdz, \qquad (8)$$

where in turn $\rho' = \rho - \hat{\rho}(z)$ and p_s is the (time dependent) surface pressure computed requiring that the depth integrated pressure perturbation is zero, that is, $\int_{-H}^0 p'dz = 0$. We assume that the hydrostatic approximation is valid[2] and note that inherent in Eq. (8) is the assumption that $\int_{-H}^0 v'dz = 0$.

As is evident from Eq. (2) estimating T_P^V alone does not provide direct information on the vertical mixing. To this end we also need information on the mixing efficiency. Nevertheless if T_P^V is small we may safely assume that very little energy is available for mixing regardless of the mixing efficiency. A differences in T_P^V from one basin to the next is nevertheless a strong indication of a similar difference in the vertical eddy diffusivity and hence vertical mixing.

3.2. The direct method

In line with most ocean models, and in particular those studying energetics of tidal motions (e.g., Carter et al., 2008; Kang and Fringer, 2012), ROMS utilizes a turbulent closure in the form of a down-the-gradient parameterization mostly to keep the model from becoming non-linearly unstable (Haidvogel et al., 2008; Warner et al., 2005). It therefore includes its own rendition of the eddy diffusion coefficient, hereafter referred to as K_m to distinguish it from K. The latter is, however, a parameterization of all unresolved scales and includes contributions from so called sub-grid scale (SGS) processes in addition to turbulence. Since ROMS is hydrostatic the most prominent SGS processes are probably non-hydrostatic processes. Hence K_m cannot be used as a direct measure of K. It is nevertheless of interest to compare the two and possibly establish a

relationship between them. If successful we may infer K directly from K_m. In ROMS there are various choices whereby K_m is parameterized. We have opted for the Generic Length Scale (GLS) parameterizations as detailed by Umlauf and Burchard (2003).

3.3. The budget method

This is the traditional method whereby the interior vertical eddy diffusion coefficient K is estimated. It is based on a simplified version of the mass conservation equation. Hence

$$K = \frac{1}{\partial_z\hat{\rho}}\int_{-H}^z \partial_t\hat{\rho}dz = -\frac{g}{\hat{\rho}N^2}\int_{-H}^z \partial_t\hat{\rho}dz. \qquad (9)$$

This expression assumes that a time averaged advection in the fjord is negligible. In closed basins during stagnant periods this is regarded as a safe assumption.

As mentioned in Section 2 there exist long term measurements of density profiles in the different basins in the Oslofjord (e.g., Berge et al., 2010). Utilizing these measurements and Eq. (9) we may therefore estimate K below sill depth in the various basins in the inner Oslofjord. An example is provided in Fig. 7 where we display a K profile at Station H3 in the Vestfjord basin. The profile is based on the time series of density profiles observed between May and August 2009.

3.4. Final remarks

The indirect and the budget methods allow us to estimate K using either model results or observed measurements as sources. Consequently we use these independent estimates to validate the model, and to study the model sensitivity to parameter choices. To this end we find that averaging independent estimates of K from several stations gives a more robust estimate for comparison. Finally we emphasize that care has to be exercised when using the direct method since the model's K_m includes parameterizations of unresolved sub-grid scale motion as well as turbulent motion.

We emphasize that the estimates based on the budget method rely on the assumption that the time rate of change of the potential density is decreasing at a steady rate at all depths. This assumption appears to be valid in the inner Oslofjord between periods of deep-water renewals (Figs. 2 and 3), and was also found to be true for recent measurements of potential density reported by Staalstrøm et al. (2012). These many independent measurements indicate that the vertical mixing in the inner Oslofjord is generated by processes that does not vary much from year to year. Breaking propagating, tidally-induced, internal waves is indeed such a process. Hence all the above measurements strongly supports the hypothesis made in the introductory section (Section 1), namely, that the energy available for mixing inside of the Drøbak Sill is dominantly due to breaking, tidally-induced internal waves.

Finally, we underscore that the ROMS version we use is hydrostatic. In view of the complicated topography, in particular in the vicinity of the main sill at Drøbak (cf. Fig. 5), a non-hydrostatic model is most likely required to properly simulate the processes responsible for transferring energy from the mean flow to the turbulent flow in particular in the vicinity of the sill region (e.g., Berntsen et al., 2008; Xing and Davies, 2007). Our focus is not on the processes in the vicinity of the sill, but rather on the energy flux radiated away from the Drøbak Sill by means of propagating, tidally-induced, internal waves. What is important to us is therefore the model's ability to approximate, to a sufficient degree, these propagating, internal waves radiating from the sill.

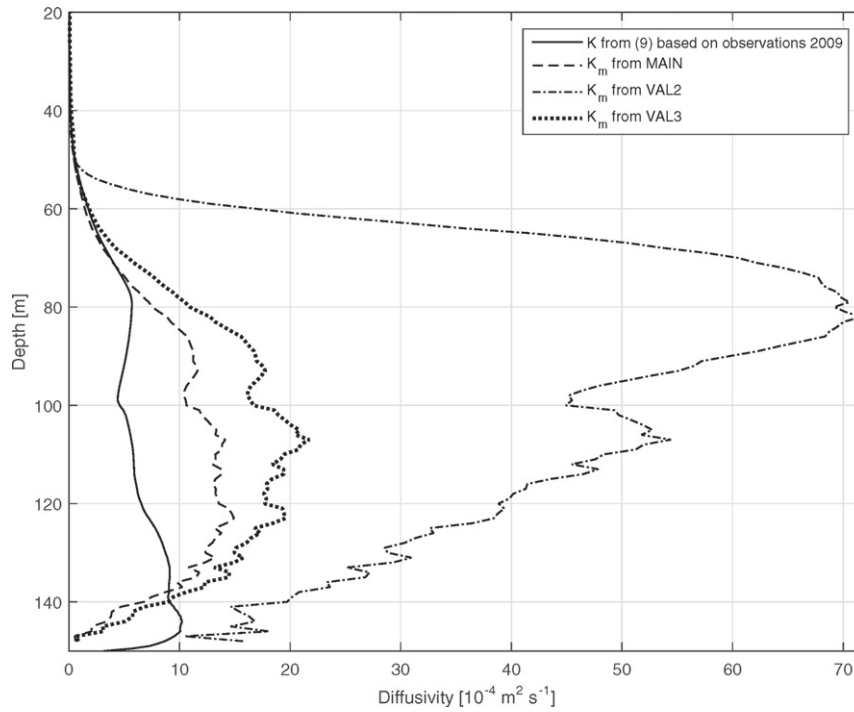[2] Note that our version of ROMS is hydrostatic.

Fig. 7. Vertical eddy diffusivity in the Vestfjord (Station H3). The solid black line is estimated using the budget method (Section 3.3) based on the observed potential density between May and August 2009.

4. The MAIN experiments

The model we use is a slightly modified version of the canonical, hydrostatic ocean model ROMS (Haidvogel et al., 2008; Shchepetkin and McWilliams, 2005, 2009). It is a public domain model featuring a generalized terrain-following vertical coordinate (Shchepetkin and McWilliams, 2003, 2005; Song and Haidvogel, 1994).

To establish a trustworthy version of the model we have performed one control run called MAIN, eight sensitivity experiments and two special experiments as listed in Table 1. The two latter are performed to show that a new vertical transform that we have developed (cf. Appendix), minimizes the infamous pressure gradient error inherent in all terrain-following models (Haney, 1991). The remaining eight investigates the impact of making changes to the parameterizations, parameters, mesh size, etc. used in MAIN.

4.1. Configuration of MAIN

The configuration of MAIN features a realistic, yet approximate, replicate of the inner Oslofjord topography and irregular coastline geometry (cf. Section 6.1 for further details). The horizontal grid mesh size is 75 m, and the number of vertical levels employed are 32. Furthermore we employ the new vertical transform and stretching function, as outlined in the Appendix, to distribute the terrain-following coordinate in the vertical. In essence the new transform is constructed so that the coordinate levels become almost aligned with the geopotential levels in the pycnocline. The sub-grid scale closure scheme is the $k - kl$ option in the GLS scheme (Umlauf and Burchard, 2003).

Initially we start from a state of rest (no motion) with a horizontally uniform specified stratification (no initial lateral density gradients). The density profile is extracted from the observations shown (Fig. 8) corresponding to the stratification denoted "medium". We note that the pycnocline is located approximately at sill depth (here 20 m), and that the stratification below 40 m depth is very weak inside of the sill. Above sill depth there are considerable variations.

The only forcing applied is a specified barotropic tide at the southern boundary of the model domain (Fig. 1). The specified tidal forcing is based on M_2 sea level with an amplitude of 20 cm, from which

Table 1
List of numerical experiments performed. The abbreviations used are Obs: Observed, Chan: Channel, Can: Canonical, that is, the default vertical transform and stretching functions (Shchepetkin and McWilliams, 2005).

| Exp.	Stratification	Transform	Mesh size	Tidal forcing	Turb. closure	Coastline	Topography
MAIN	Medium	New	75 m	M_2	$k - kl$	Real	Real
PGE1	Strong	Can	75 m	None	$k - kl$	Real	Real
PGE2	Strong	New	75 m	None	$k - kl$	Real	Real
VAL1	Obs	New	150 m	Obs	$k - kl$	Real	Real
VAL2	Obs	Can	75 m	Obs	$k - kl$	Real	Real
VAL3	Obs	New	75 m	Obs	$k - \epsilon$	Real	Real
REA1	Obs	New	75 m	Obs	$k - kl$	Real	Real
REA2	Weak	New	75 m	M_2	$k - kl$	Real	Real
IDE1	Obs	New	75 m	M_2	$k - kl$	Chan	Idealized
IDE2	Obs	New	75 m	M_2	$k - kl$	Chan	Idealized
IDE3	Obs	New	75 m	M_2	$k - kl$	Chan	Real
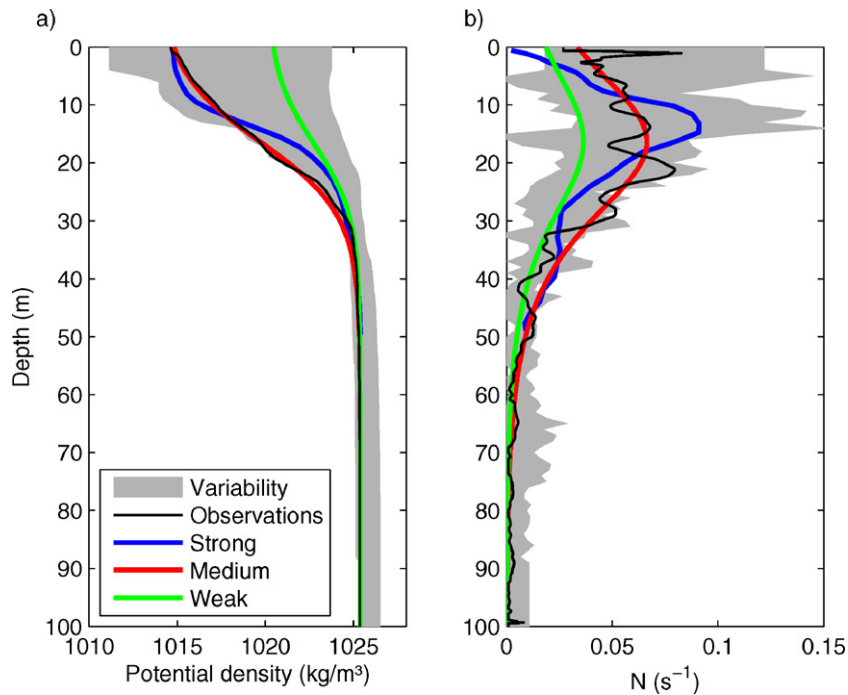
Fig. 8. Potential density (a) and corresponding Brunt–Väisälä-frequency (b) used in the model runs. The profiles are based on measurements from Station S2 as described in Staalstrøm et al. (2012). The gray shaded areas indicate the maximum and minimum values during 2008 and 2009. The solid green, red and blue line is referred to as a "weak", "medium" and "strong" stratification, respectively, in accord with its effect on the Brunt–Väisälä-frequency in the pycnocline. The black line is an example of an instantaneous observed profile taken August 18 2009.

is calculated the barotropic tidal velocity component into the fjord (v_{BT}) using the continuity equation. Specifically

$$v_{BT} = \int_{-H}^{0} v \, dz = \frac{Y}{A} \partial_t \zeta \qquad (10)$$

where Y is the horizontal area of the fjord inside of the open boundary, A is the cross section area of the open boundary and ζ is the sea level averaged over the horizontal area inside this boundary. The tides are spun up over a period of 12 h during which the forcing is ramped up using a hyperbolic tangent function which returns zero for the first 6 h.

Regarding the barotropic tide the distance between the two stations is too small to be of any significance.

4.2. Evaluation of results from the MAIN experiment

The model experiment REA1 are similar to MAIN, except REA1 use the observed stratification and sea level. The stratification termed "medium" is a smoothed version of the observed, and the observed sea level is close to a sine curve with amplitude 20 cm. We start by comparing the observed tides at Oslo Harbor to those generated by the model by using observations at Kaholmen (REA1), which is located well inside of the southern boundary (Fig. 9). Regarding barotropic tide the distance between the station Kaholmen and the open boundary is too small to be of any significance. As revealed the differences in sea levels in REA1 and observations are small, indicating that the model is doing satisfactory well regarding the tidal signal.

To assess how well the model results reproduce observed currents we compare them with observed time series of baroclinic currents at Stations S2 and S5 (Fig. 1). We choose these stations since they are located, respectively, 1 km and 10 km inside of the sill,

and are sufficiently separated to ensure a fair estimate of the internal wave energy flux. The observations are extracted from the 2009 measurements reported by Staalstrøm et al. (2012) and covers the 24 hour period (two tidal cycles) starting August 18, 2009 at 08UTC. The 24 hour period model results are extracted from a 2.5 day simulation to cover two maxima in the tidal currents well after the 12 hour spin up period. As revealed by Fig. 10 the strength of the inflow and outflow speeds of the currents extracted from REA1 at Station S2 is almost the same as the observed ones, but the REA1 simulated inflows are located somewhat deeper than the observed ones. At Station S5 the REA1 simulated inflowing speeds are considerably weaker and deeper, while the outflow speeds are both stronger and deeper than those observed. Possibly this difference is caused by a barotropic inflowing component in the observations caused by processes not present in the pure tidally forced simulations, e.g., wind forcing. This conjecture is supported by the fact that Station S2 is closer to the sill where the tidal signal dominates the motion.

Also shown by Fig. 10 are estimations of the total internal wave energy fluxes through these sections both from the model and the observations using the indirect method (cf. Section 3.1, Eq. (7)). The resulting REA1 energy flux is estimated to 245 kW at Station S2 and 43 kW at Station S5 corresponding to a loss of 202 kW between the two stations. The similar numbers for the observed energy flux are 277 kW and 73 kW, representing a loss of 204 kW. The latter is remarkably close to the modeled one. Percentagewise the losses differ somewhat though with a simulated loss of 82% compared to an observed loss of 74%. The simulated loss is nevertheless not significantly higher than the observed one.

Included in Fig. 10 are also time series of the depth of selected isopycnals. Inspection of these indicates a difference in the vertical displacement of the observed and modeled isopycnals, e.g., the 1022 kg m^{-3} isopycnal, the observed ones being higher at both

stations. Despite this difference the difference between the two stations is striking and similar in observations and the REA1 simulation. This is in line with the remarkable similarity in the losses in energy fluxes.

In summary we conclude that the model reproduces the response due to the tidal forcing satisfactorily. Instead of using observed sea level at the open boundary, MAIN uses a sine curve with equal amplitude and return very similar results. Hence we may use the results from the latter experiment to investigate variabilities in the turbulence production inside of the sill, and thereby get insight into possible differences in the eddy diffusion coefficient or local vertical mixing in the various fjord basins. To further corroborate this conclusion we have performed the eight sensitivity experiments listed in Table 1. We comment on the results of the latter when appropriate.

5. Results

5.1. Turbulence production and eddy diffusivity

We split the inner Oslofjord into four basins referred to as Basins H2–H5 where H4 correspond to the Vestfjord basin and H5 correspond to the innermost Bunnefjord basin(Fig. 11). These basins and their cross-sections are carefully chosen to ensure that they have comparable depths and a sufficient lateral separation (cf. Section 6.3). To estimate the turbulence production, T_P^V, in each basin by the indirect method, that is, by Eq. (5), we first need to compute the wave energy flux through the various sections bounding the each basin. To this end we use Eq. (7). The results for the MAIN and the REA2 experiments are given Table 2.

As revealed by Table 2 the turbulence production decreases as we proceed into the fjord. Moreover, the lowest production is in the innermost basin (H5) indicating that very little wave energy is available for vertical mixing in the innermost basin. Hence we expect the eddy diffusivity to be small there as well. Furthermore, the turbulence production is about six times higher in the Vestfjord basin (H4) than in the Bunnefjord basin (H5) supporting the notion that the Bunnefjord basin is far more vulnerable regarding the possibility of developing hypoxic events.

Table 2 also disclose results from experiment REA2, which differ from MAIN in that its initial stratification is the one denoted "weak", that is, a stratification with a much less pronounced pycnocline (cf. Table 1 and Fig. 8). As exhibited applying a weaker pycnocline results in lower turbulence productions. The pattern is maintained though, which suggests that the decrease in production as we proceed into the fjord is a robust signal and independent of the initial stratification.

What about the eddy diffusion coefficient K? To calculate it we use the budget method, that is, Eq. (9) and observations from the four stations H2–H5 located in the center of each of the respective basins. Furthermore we take the mean of K in the depth range 90 m to 125 m. The rationale is that below this depth each basin forms a closed basin allowing us to separate them. Furthermore, K is fairly constant throughout this layer (Fig. 7) and is probably the layer where most of the vertical mixing takes place. The results are listed in Table 3, and clearly reflect the conclusion that very little mixing takes place in the innermost basin compared to the basins closer to the Drøbak Sill, that is, Basins H4 and H2.

We recall from Eq. (2) that the turbulence production does not give the whole story regarding vertical mixing. How much of the production left for mixing depends on the the mixing efficiency in each basin. Recall that the mixing efficiency is $R_f = N^2 K / T_P^V$ or $K = T_P^V R_f / N^2$. Hence we may use the results given in Tables 2 and 3 to study whether there is a possible linear relationship between the turbulence production and the eddy diffusivity. To this end we have plotted, as depicted in Fig. 12, the estimated values of K against the estimated turbulence productions for each basin. As revealed they do not fall on a straight line, suggesting that the mixing efficiency differs from basin to basin. Nevertheless Fig. 12 leaves the impression that an increase in turbulence production gives rise to a similar increase in the eddy diffusivity. However, to infer the eddy diffusion coefficients directly by use of the indirect method, that is, from Eq. (2), assuming that R_f is invariant from basin to basin is dubious. Finally, it is interesting that the mixing efficiency in the Vestfjord basin (H4) appears to be higher (compared with a linear relationship) than in the other basins. The result is that more of the turbulence production is used to enhance the mixing in this basin. This may be related to the contribution by the reflected waves as discussed further in Section 5.2.

5.2. Wave reflection

Based on observations Staalstrøm et al. (2012) found that the ratio between the potential and kinetic energy density in a two-layer progressive interface wave was higher than unity at Station S2 and less than unity at Station S5. They interpreted this to imply that the dominant internal wave is not purely progressive and that some reflection of energy takes place. It is therefore of interest to investigate whether this is reflected in the model results. To this end we use the results emanating from MAIN. Recall that in MAIN the stratification used is the medium one displayed in Fig. 8, and that the M_2 forcing is 20 cm.

As a measure we use the vertical displacement of individual isopycnals away from their initial depth z and investigate how it changes in time and space. The displacement $\eta(x,y,z,t)$ is (Gill, 1982, page 140, Eq. 6.7.4)

$$\eta = -(\rho - \hat{\rho})(\partial_z \hat{\rho})^{-1}. \tag{11}$$

The wave propagation is perhaps best viewed in a Hovmöller diagram (Fig. 13) in which the horizontal axis is along a path that starts south of the Drøbak Sill and ends in the northern part of the Vestfjord basin (Fig. 14). Shown is the displacement at 25 m. The wave clearly propagates as a first baroclinic mode, internal wave with a phase speed of about 0.8 m s^{-1}. Moreover, a reflected wave at the northern end is disclosed which may well lead to the enhanced mixing in the Vestfjord basin alluded to in the previous section.

Also apparent in Fig. 13 is a marked decrease in the wave amplitude as it propagates into the fjord, and is an alternative way to display that wave energy is lost as we proceed into the fjord. This is perhaps even better illustrated by Fig. 14 depicting the spatial distribution of where turbulence is produced by displaying the spatial variation in amplitude of the displacement η at 25 m depth. As disclosed the amplitude is more than 7 m just inside of the Drøbak Sill and exhibits a decrease to just below 1 m in most of the Vestfjord basin (H4). In the Bunnefjord basin (H5) it is less than 0.5 m. The higher amplitudes are found in the shallower areas between the Vestfjord and Bunnefjord basins indicating reflection and/or enhanced wave breaking. A similar effect appears at the southern end of the Bunnefjord basin.

Stigebrandt (1976) estimated the energy flux away from the Drøbak Sill to be 600 kW forced with a M_2 sine wave with an amplitude of 15 cm, by assuming a progressive wave with no reflections. The presence of wave reflection explains why the present estimated energy flux is lower by a factor of at least 2 (Table 2).

6. Discussion

The above results clearly shows that the vertical mixing due to breaking of propagating, tidally-induced internal waves decreases as
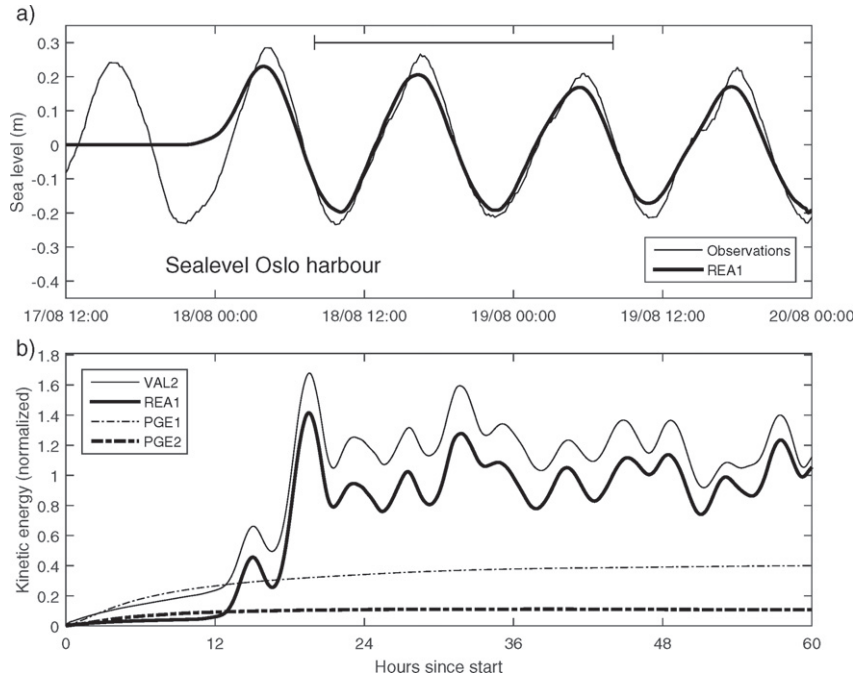
Fig. 9. Upper panel (a) displays time series of the observed sea level at Oslo Harbor (solid thin line) and the similar time series extracted from the results of the REA1 experiment (solid thick line). Atmospheric forcing is removed by performing a running mean value over two tidal cycles and then subtract the result from the observations. The same procedure is applied to the forcing at the open boundary of the model. Lower panel (b) displays time series of the volume averaged kinetic energy extracted from REA1 (solid thick line), VAL2 (solid thin line), PGE1 (dashed thin line) and PGE2 (dashed thick line). Time is indicated along the horizontal axis. Note the 12 hour spin up time evident in the time series from the numerical experiments.

we proceed into the fjord. It also shows that very little energy is available for mixing in the innermost Bunnefjord basin. The question arising is how robust the results are? What happens if we for instance change the resolution, make changes to the topography, the irregular coastline geometry, the turbulence closure scheme, strenght of the tidal input and the initial stratification?
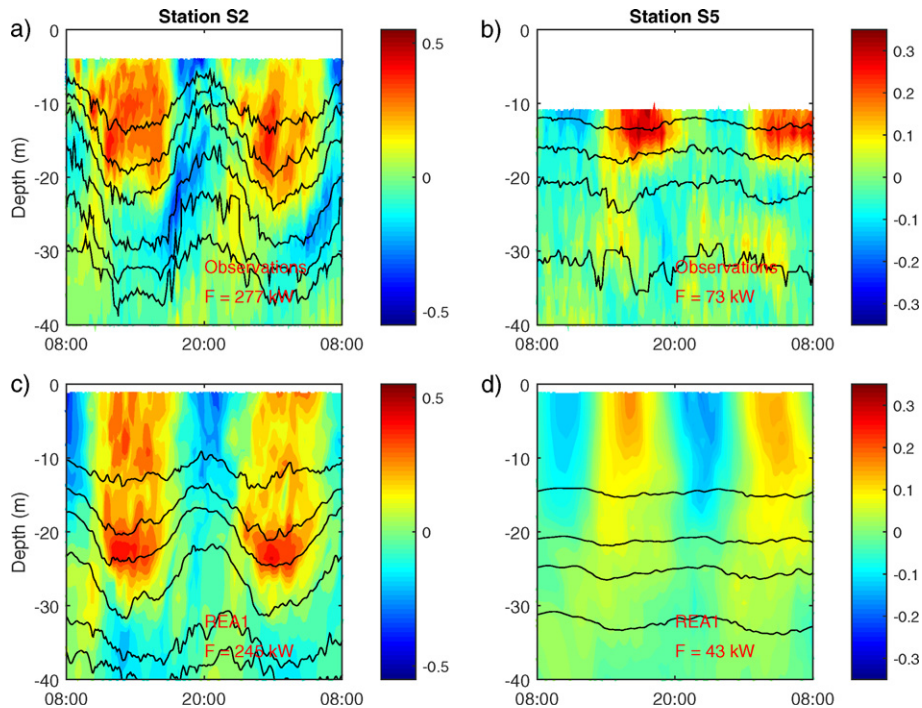

Fig. 10. Displayed is the 24 hour time evolution starting August 19, 2009 at 08UTC of currents and selected isopycnals at Station S2 (left column) and S5 (right column). Panels a) and b) are based on observations and panels c) and d) on results from REA1. At Station S2 isopycnals 1018, 1020, 1022, 1024, 1025 and 1025.25 psu are drawn and at Station S5 the 1019.1, 1022, 1023.6 and 1024.8 psu isopycnals are drawn. Baroclinic current speed estimated using Eq. (8) is indicated by the color bar (m s^{-1}). Positive values (red) are currents directed into the fjord, and negative values (blue) are currents directed out of the fjord.
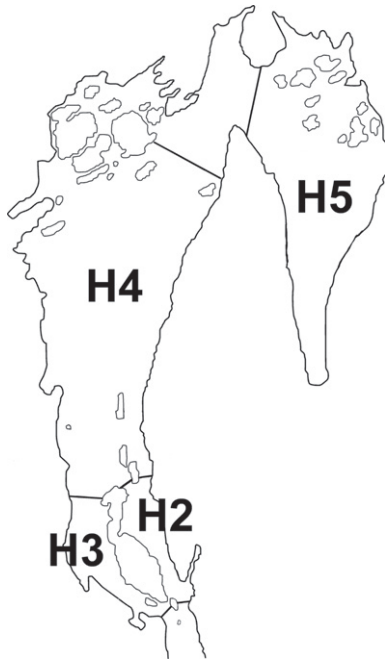
Table 3
The eddy diffusivity coefficient in the Basins H2, H3, H4 and H5 calculated using the three different methods of Section 3. All numbers are in cm^2 s^{-1}.

Basin				
Method	H2	H3	H4	H5
Budget	~20	~3	~5	~1
Indirect	19.8 ± 6.0	5.4 ± 0.1	2.4 ± 6.0	1.7 ± 0.1
Direct	22.7	15.2	11.2	10.9

Fig. 11. The internal wave energy flux in seven selected cross sections of the fjord is calculated from Eq. (7) for a medium (MAIN) and weak (REA2) stratification (Table 2), separating four different basins in the Oslofjord labeled H2, H3, H4 and H5.

6.1. Resolution and topography

The large variations in the topography, including the underwater barrier and the Drøbak Sill itself with its minor sills, present a challenge. In fact we have manually edited the Drøbak Sill to maintain a sill depth of 20 m, and to conserve the cross section area over the sill in the eastern part. Moreover, because of the shallowness of the underwater barrier we have chosen to replace it by landcells, except for the two narrow openings. This effectively hinders the east–west exchange south of the Håøya. Further north at Stations R1 and R2 (Fig. 4) the sounds between the islands are narrow and V-shaped in depth. To ensure that the smoothing process does not produce spurious sills the depths are deepened manually in these particular grid-cells. Note that all grid configurations, including MAIN, are smoothed to get a maximum roughness factor of 0.2 satisfying the hydrostatic inconsistency criterium associated with terrain-following coordinate models (Haidvogel et al., 2008; Haney, 1991; Shchepetkin and McWilliams, 2003).

A first impression of the importance of resolving the topography is displayed by Fig. 4. It reveals that the 75 m model version more or less mimics the observed topography (25 m mesh size) while the 150 m set-up does not. This is further quantified and corroborated by the spectra shown in Fig. 15 in which the power spectrum of the topography using a 25 m mesh is compared to the topography spectra of the 75 m and the 150 m meshes. As depicted the wavelengths longer than 700 m are all well captured by the 75 m set-up,

while the 150 m grid resolution model only captures wave-lengths longer than 2 km. Apparently the 75 m version resolves fairly well the dominant topographic features in the vicinity of the sill, while the 150 m version does not. Hence we suspect that the 75 m grid resolution version will fair better compared to observations, in particular with regard to the internal wave energy fluxes.

When we increase the mesh size to 150 m, as is done in the VAL1 experiment (Table 1), the estimated internal wave energy flux at Station S2 is reduced to 153 kW, while the estimate at Station S5 is only reduced to 39 kW (Fig. 16) corresponding to a reduced energy loss of 114 kW (75%). As revealed by Fig. 16 these numbers are reflected in the baroclinic speeds at Stations S2 and S5. Whereas those at Station S2 are substantially reduced those at Station S5 are more similar to those of the MAIN experiment. We attribute the reduction in current speeds and energy flux to the fact that the topography close to the sill (Station S2) is not well represented in the VAL1 experiment.

6.2. Strength of the tidal input

Fig. 17 shows how the vertical displacements vary as a function of the strength of the elevation of the tidal input, here varying in the range 5 to 25 cm, using results from the MAIN and the REA2 experiments. Recall that REA2 differs from MAIN in that it employs a weaker stratification (less steep pycnocline).

As displayed both MAIN and REA2 underestimate the amplitudes, but MAIN more so than REA2. The latter is expected since a weaker stratification enhances the vertical displacements of an isopycnal for the same energy input. We also note that the amplitudes increase as the tidal input gets stronger in line with the observed amplitudes. We also note that the amplitudes at Station S2 are much higher than at Station S5, an independent indication that the tidally-induced propagating, internal waves indeed loose much of their energy between the two stations. Thus another measure of how well the model reproduces the turbulence production is to calculate the decrease in the amplitude of the 1022 kg m^{-3} isopycnal between Stations S2 and S5. In fact the modeled and observed ratio between the amplitudes at Stations S5 and S2 is very similar being 0.22 ± 0.03 using results from the MAIN experiment and 0.25 ± 0.04 using observations.

6.3. The effect of employing an irregular coastal geometry

When we use the indirect method to estimate the eddy diffusion coefficient by means of Eq. (4) through Eq. (7), we rely on a trustworthy estimation of the average turbulence production in an
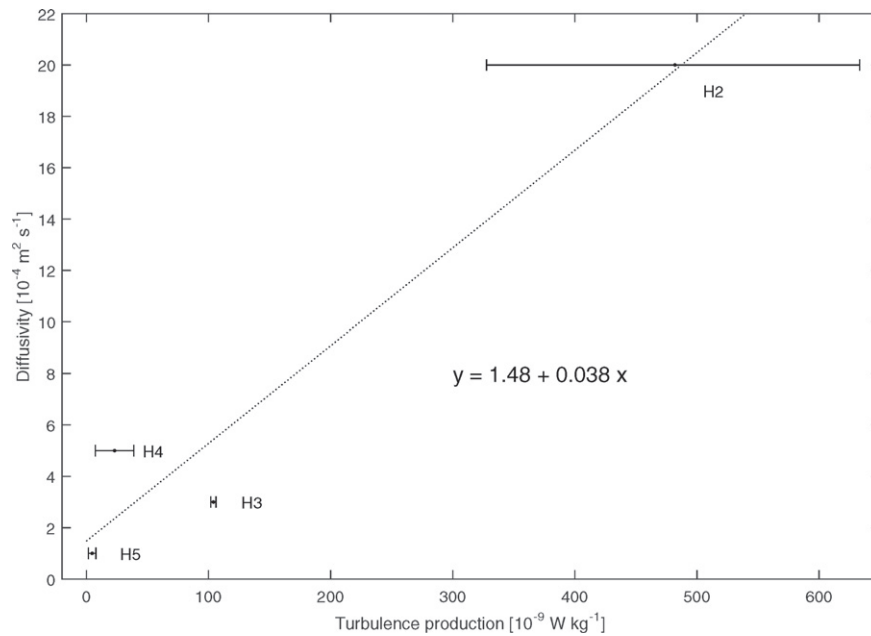
Table 2
The net internal, wave energy fluxes through the cross-sections bounding the four Basins H2–H5 displayed in Fig. 11. All energy fluxes are in kW, and T_P^V is in 10^{-9} W kg^{-1}. They are calculated by use of Eq. (5). MAIN and REA2 refer to two of the experiments listed in Table 1 and differ only in the initial stratification applied.

Basin								
	H2		H3		H4		H5	
Exp.	MAIN	REA2	MAIN	REA2	MAIN	REA2	MAIN	REA2
F_1	297	130	78	26	123	28	15	3
F_2	96	26	53	2	26	5	0	0
T_P^V	633	328	106	102	31	7	8	2

Fig. 12. The eddy diffusion coefficient (diffusivity) as a function of turbulence production in the four different Basins H2–H5 in Fig. 11. The diffusivity is calculated from Eq. (9) based on observations of density, and is an average over the depth range 90 to 125 m. The turbulence production is calculated from Eq. (5) based on the modeled energy fluxes shown in Fig. 11. In Eq. (7) the volume below 20 m in each basin is chosen. The size of the black points indicates the volume of each basin, and the black line is a least square fit to the four data points.

enclosed volume *V*. In particular the result depend on how well the boundary Ω encompassing the volume *V* is represented in the model. It is therefore of interest to investigate the effect of employing a fjord featuring an idealized regular coastline geometry in the form of being a straight channel with parallel walls.

Consequently, in the three experiments IDE1, IDE2 and IDE3 (cf. Table 1), we replace the irregular coastline geometry by straight channel walls. Furthermore, we let the topography varies singularly in the direction into the fjord. All three experiments employ a

horizontal mesh size of 75 m. Finally, we let the topography variation into the fjord in IDE3 mimic the topography of MAIN inside of the Drøbak Sill, while IDE1 and IDE2 use either a single sill configuration (IDE1) or a two sill configuration (IDE2) as depicted in the upper right-hand panel of Fig. 18. For comparison Fig. 18 also shows the depth profile along the the transect shown in Fig. 14 used in MAIN (upper left-hand panel of Fig. 18). With this configuration the area inside of the southern boundary is drastically reduced leading to a drastically reduced barotropic tidal current input as given by Eq. (10)
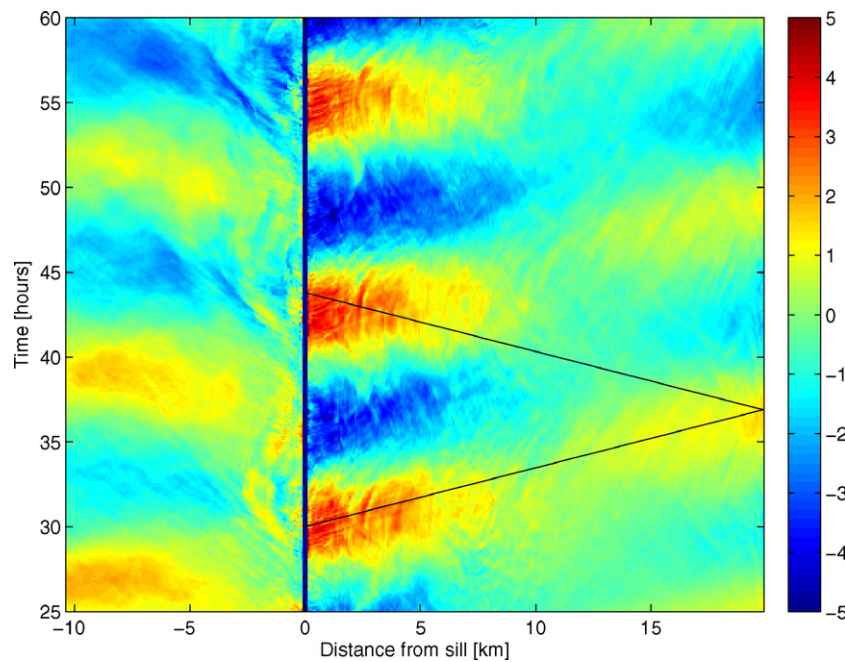

Fig. 13. The vertical displacement at 25 m as a function of time and space along a south–north transect of the Oslofjord. The distance indicated along the horizontal axis is the distance from the Drøbak Sill, while time in hours is indicated along the vertical axis. The hours correspond to the hours displayed in Fig. 9. The path of the south–north transect is shown in Fig. 14. The black line indicates a phase speed of 0.8 m s^{-1}.
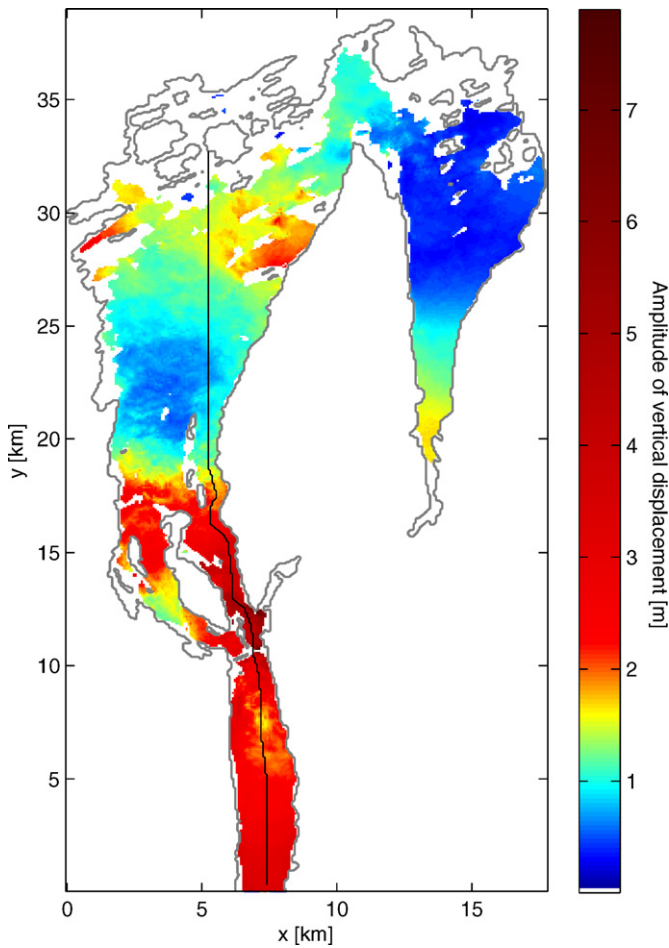
We conclude that the depth profile and the inclusion of a realistic, irregular coastal geometry is important for the estimation of the internal wave energy flux loss and hence for the estimation of the turbulent production. The results however show that care must be exercised when choosing the volume over which we estimate and compare modeled and observed energy fluxes when evaluating the model results. To avoid the problem we have therefore limited our comparisons to cross sections where the maximum depths are comparable in the results shown in Section 5.

6.4. Turbulence closure scheme

As alluded to in Section 3.2 it is tempting to use the model's rendition of the vertical eddy diffusion coefficient, K_m, as a measure of the actual eddy diffusivity, K. This is however not straightforward in that K_m includes contributions from the sub-grid scale motion, here mostly non-hydrostatic effects, as well the turbulent motion. Thus we expect K_m to be larger than K.

Since the model is equipped with more than one closure model, we have performed experiments with two of them, namely the $k - kl$ closure as used in the MAIN and the VAL2 experiments and the $k - \epsilon$ closure as used in the VAL3 experiment, to study their effect on the eddy diffusivity. Based on the density difference measured at Station H4 in the southern end of the Vestfjord basin (Basin H4) between May and August 2009, the estimated value of K is $5 \cdot 10^{-6}$ m² s⁻¹ (Fig. 7) at 25 m depth. The modeled diffusivity K_m averaged over the Basin H4 volume gives $6 \cdot 10^{-6}$ m² s⁻¹ when we use the $k - kl$ closure model (MAIN) and $8 \cdot 10^{-6}$ m² s⁻¹ when we use the $k - \epsilon$ closure model (VAL3). These values appear to fit well with the independent estimates made by Bjerkeng et al. (1978).

Furthermore we have, by the use of the budget method, calculated the depth profile of K based on the observations at Station H4 and compared it with the similar depth profile of K_m based on the model results from MAIN, VAL2 and VAL3 (Fig. 7). Recall that VAL2 differs from MAIN in that it uses the canonical vertical transform that leads to unacceptable current levels due to the pressure gradient error, while VAL3 differs from MAIN in that it uses the $k - \epsilon$ instead of the $k - kl$ closure scheme. We observe that the shape of the observed and modeled profiles between 20 and 50 m depth is quite similar. Furthermore we notice that the profiles based on MAIN and VAL3, although being on average two times larger than the observed one below 70 m, much better represent the observed diffusivity profile than the profile based on VAL2 results. This emphasizes the importance of minimizing the pressure gradient error as done in MAIN and VAL2. Finally we emphasize that the diffusivity cannot be calculated from the budget method above 20 m which is why Fig. 7 stops at 20 m depth.

To conclude it appears that vertical diffusivity gets large in areas where there are large artificial currents due to the pressure gradient error. Hence the vertical diffusivity appears to be sensitive to the choice of the vertical transform and stretching functions. In contrast the modeled vertical diffusivity is less sensitive to the choice of turbulence closure model. It also appears that there is a relationship between K_m and K, particularly in the depth range 90 to 125 m, except that K_m as expected is biased toward higher values. Nevertheless we do not recommend to use the model's rendition of the eddy diffusivity as a measure of the real one.

6.5. The effect of weak and strong stratification

In MAIN we initialized the model with the smoothed observed density profile referred to as "medium" stratification (Fig. 8) with a maximum Brunt–V äisälä-frequency of $N^2 \sim 0.07$ s⁻¹. In the same graph a density profile with a maximum $N^2 \sim 0.03$ s⁻¹ referred to as "weak" stratification is also plotted. As is well known (e.g, Bell, 1975; Jayne and Laurent, 2001) a reduced pycnocline slope, or rather

Fig. 14. The amplitude of the vertical displacement at 25 m depth as calculated from Eq. (11). The color scale enhances gradients at relatively small ranges. The black lines indicate the transect along the fjord used in Fig. 13.

which explains the substantial reduction in the energy levels in the three IDE experiments compared to MAIN as disclosed by two lower panels in Fig. 18.

A comparison of the wave energy fluxes estimated using Eq. (7) reveals that the most striking difference between those fluxes generated by MAIN and those generated by IDE1–IDE3 are the expected reduction in the maximum to about on tenth (Fig. 18) as explained in the previous paragraph. Comparing MAIN and IDE3, that both features a replica of the real topography, both show a similar pattern. Within the first 6.5 km there is considerable variability, and the local maxima and minima in the flux correlate well with local minima and maxima in the depth profile. Further away from the sill the energy flux in both experiments levels out and become nearly constant. Furthermore, within the first 6.5 km the flux decreases overall corresponding to a major loss of energy. This is different from the pattern associated with two other IDE experiments in which a more idealized topography is used. In IDE1 (one sill only) the energy level first increases downstream of the sill before it slowly declines. When the second sill is introduced (IDE2) the energy flux increases downstream of the first sill, declines just upstream of the second sill before increasing again further downstream. We suspect that the negative correlation between the energy flux profile and the bathymetry could be caused by the method in which the energy flux is calculated. In Eq. (8) it is assumed that the barotropic mode is equal to the depth-averaged mode, and this is maybe not a valid assumption, leading to a depth dependence in the calculated energy fluxes.
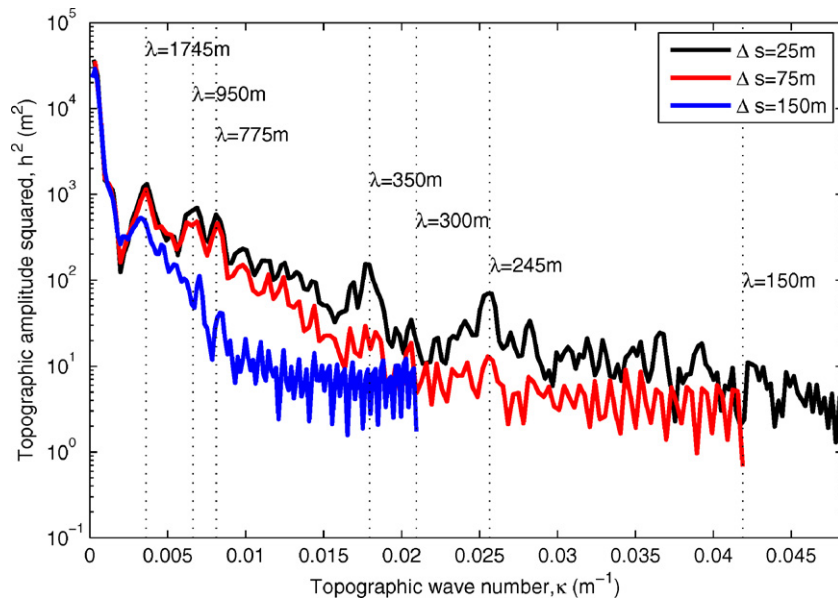
Fig. 15. Comparison of observed and model bathymetry spectra. The black line is the spectrum of the observed bathymetry (5m grid resolution), while the red and blue lines show the spectra of the 75m and 150m model topography, respectively. Note that the spectrum of the 75m grid resolution model pretty much follows the observed topography spectrum, while the 150m grid resolution model falls below the observed one already at wave lengths above 1745m.

a reduced density difference between the upper and lower layers, the amplitude of the internal waves increases, but not necessarily the energy flux. Reducing the stratification is therefore expected to give less energy available for turbulence production further into the fjord.

As an example we compare two model runs MAIN (medium stratification) and REA2 (weak stratification) both forced with a M_2 tide of amplitude 20 cm. At Station S2 the amplitude of the vertical displacement at 20 m depth is about 5.6 m and an the energy flux is about 130 kW for the REA2 experiment. In the MAIN experiment the amplitude is reduced to 4.3 m whereas the energy flux is *increased* to 297 kW. A similar difference is found also for other forcing amplitudes of the surface elevation at the southern boundary as displayed in Fig. 17.

7. Summary and final remarks

It has long been known that the innermost basin of the inner Oslofjord, known as the Bunnefjord basin, experiences long periods of hypoxic to anoxic events that have a dramatic effect on the ecological environment (Beyer and Føyn, 1951). This is commonly

attributed to a weak vertical mixing, a mixing that is much weaker than in the basins closer to the sill (Baalsrud et al., 2002; Berge et al., 2010; Dolven et al., 2013; Gade, 1970). In fact the weak mixing obstructs any frequent deep water renewal to take place, and hence the water becomes stagnant. The question that immediately arises is why the local vertical mixing in the innermost basin is weaker than in the other basins closer to the sill. Our hypothesis, which was first formulated by Stigebrandt (1976) based on the results reported by Gade (1970), is twofold:

1. Mixing in the inner Oslofjord is predominantly due to turbulence production caused by breaking of tidally-induced, propagating internal waves whose source region is the sill at Drøbak
2. The internal wave energy left for mixing in the innermost basin is small.

To confirm the hypothesis we combine modeling and analyses of observations. The model we employ is a hydrostatic version of the ocean model ROMS implemented for the inner Oslofjord. To properly resolve the complex topography and irregular coastline geometry of the fjord we find that a mesh size of 75 m is necessary. To generate
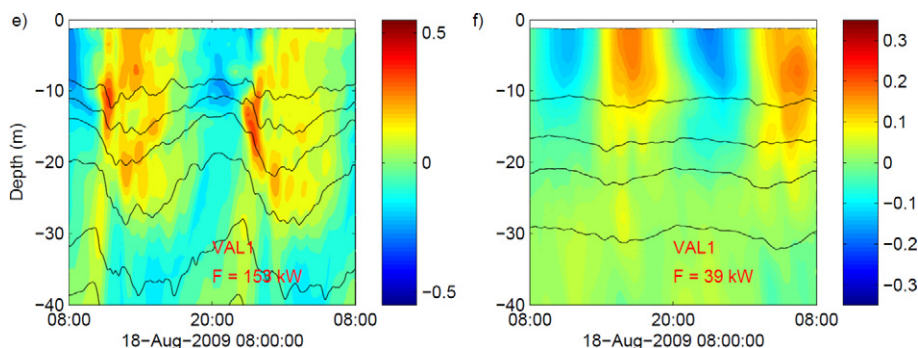

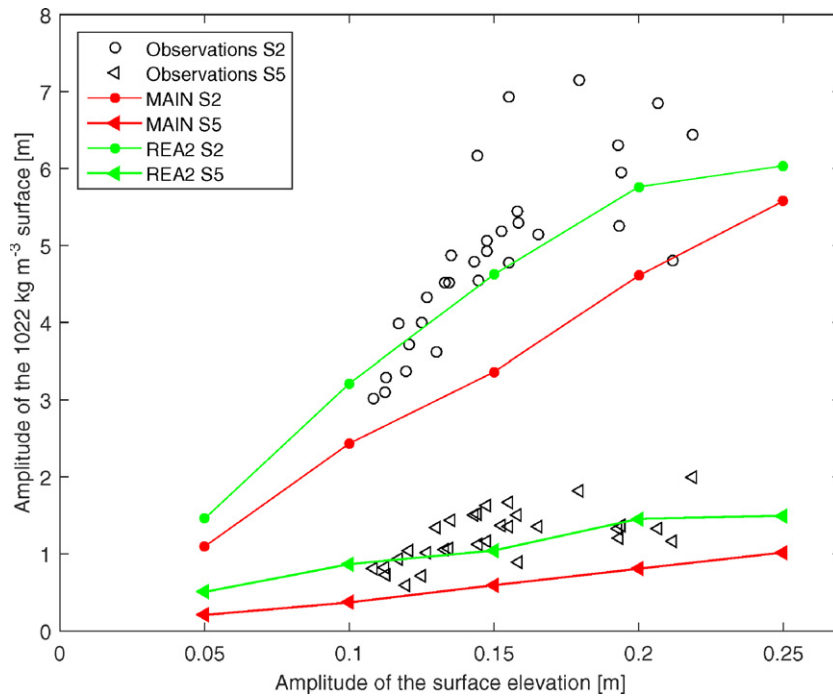**Fig. 16.** Same as Fig. 10, but for the VAL1 experiment.

Fig. 17. Amplitude of the vertical displacement of the 1022 kg m^{-3} isopycnal as a function of the surface elevation amplitude. Open circles and triangles denote observations from Stations S2 and S5, respectively. Closed circles and triangles are similar results emanating from a simulation using a fully three-dimensional barotropic/baroclinic ocean model.

tidally-induced, propagating internal waves we force the model by specifying the barotropic tides at the model's southern boundary located well south of the major sill at Drøbak. The model is initialized

with a laterally, uniform stratification smoothed version of observations made by Staalstrøm et al. (2012). A number of sensitivity experiments are performed to get insight into the model's sensitivity
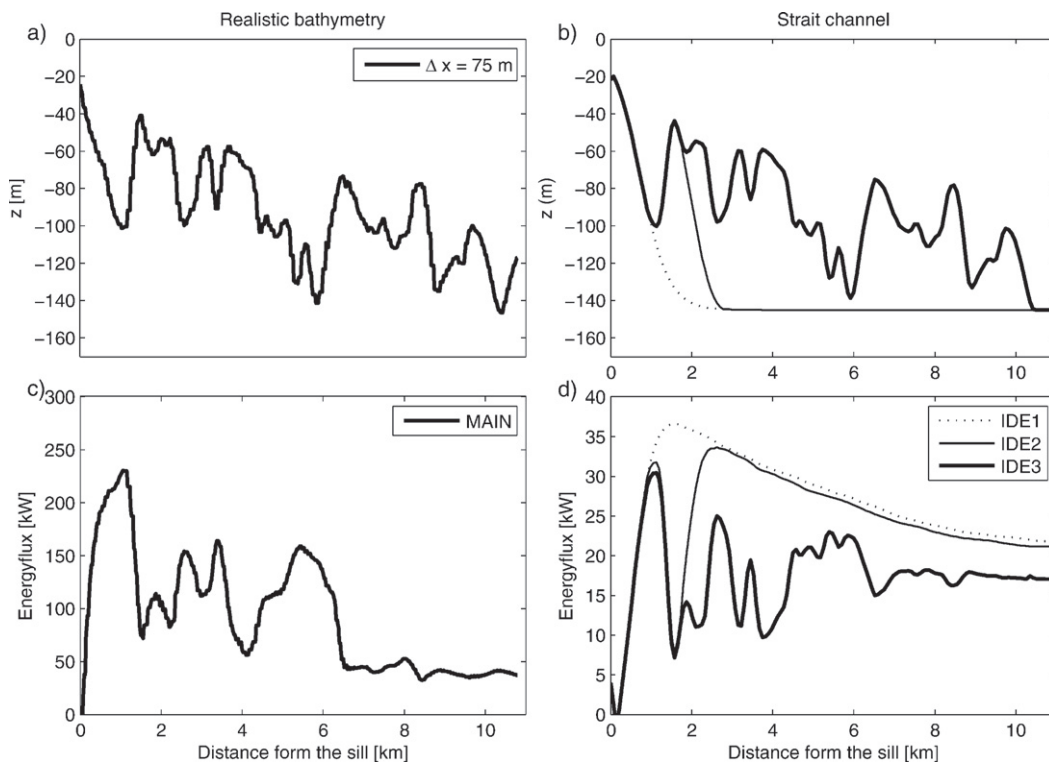

Fig. 18. Depth profiles (upper two panels) and associated estimates of the internal wave energy fluxes (lower two panels) into the fjord as estimated from Eq. (7). The left-hand column shows results from the MAIN experiment, while the right-hand column depicts results from the idealized experiments IDE1, IDE2 and IDE3. Solid thick line is associated with the IDE1 experiment, solid thin line with the IDE2 experiment and dotted line with IDE3 experiment. The different bathymetry configurations in IDE1, 2 and 3 are drawn on top of each other.

to various parameters, parameterizations, and mesh size. We note that the method we use is generic, and may be applied to any sill fjord to study spatial variations in the vertical mixing and turbulence production due to breaking of propagating internal waves.

We use the local vertical eddy diffusivity or vertical eddy diffusion coefficient K as a measure of the vertical mixing. To estimate K we employ three methods. The first is the indirect method in which the net turbulence production within four basins in the Oslofjord is estimated using a version of the method outlined by Nash et al. (2005). The turbulence production is related to the vertical diffusivity as outlined in Section 3.1, but requires knowledge of the so called mixing efficiency. The second method is the direct method in which we explore using the model's rendition of the diffusivity as a measure for K (Section 3.2). The third and final method is the classical budget method (Section 3.3).

We find that the propagating, tidally-induced internal waves may indeed explain differences in mixing between the Vestfjord basin (Basin H4) and the innermost Bunnefjord basin (Basin H5). In fact the indirect method reveals that the turbulence production in the basin closest to the sill (Basin H2) is as large as $633 \cdot 10^{-9}$ W kg^{-1}. Proceeding into the fjord it decreases to $31 \cdot 10^{-9}$ W kg^{-1} for the Vestfjord basin (Basin H4). In contrast only $8 \cdot 10^{-9}$ W kg^{-1} is available for mixing in the innermost Bunnefjord basin. This is compared to estimated eddy diffusivities based on the budget method and observations. The method returns $\sim$20 cm^2/s in Basin H2, $\sim$5 cm^2/s in Basin H4 and $\sim$1 cm^2/s in the innermost basin (Basin H5).

By comparing eddy diffusivities and turbulence production (Fig. 12) it is evident that the mixing efficiency of the basins is different. Thus there is no direct universal relationship between turbulence production and eddy diffusivity. Furthermore we find that the model's rendition of the eddy diffusivity averaged over the basins is of the same order of magnitude as the observed ones.

Finally we remark that the only forcing applied is sea level variations at the southern boundary of model domain, where the barotropic flow is calculated from Eq. (10). The result is a baroclinic signal in the form of propagating internal waves inside of the Drøbak Sill. When observed sea level is used as forcing, the model is able to reproduce the observed sea level at the fjord head remarkably well (cf. Fig. 9). When the model is forced with a sinusoidal sea level with varying amplitude, we find that there is a linear relationship between the amplitude of the sea surface elevation and the vertical displacement of density surfaces around sill depth (Fig. 17). This is in line with findings of Staalstrøm et al. (2012) based on observations.

There are also many other sources than tides that may create baroclinic signals. This could be fresh water inflow, wind stress at the surface and barotropic signals of meteorological origin (e.g., storm surges). The wind is clearly important for the surface current during strong winds, and can cause even greater modifications in the flow due to mixing of the upper layer. In our experiments the wind stress is set to zero. Hence when comparing model results and observations we carefully choose a period with relatively weak winds. The effect of episodes of strong winds and fresh water inflow is only included indirectly in experiments deviating from the MAIN by using stratifications similar to measured stratification after such episodes as initial conditions in the model run.

Appendix A. A new vertical transform and stretching

Like all models featuring a terrain-following vertical coordinate our Oslofjord version of ROMS is prone to the infamous pressure gradient error (PGE) (e.g., Berntsen and Thiem, 2007; Shchepetkin and McWilliams, 2003). Our Oslofjord version of ROMS is especially exposed due to the complicated and highly varying topography combined with strong stratification.

The PGE is generated when transforming the lateral pressure forcing in the momentum equation, that is,

$$\partial_x p|_z = -g \int_z^0 (\partial_x \rho|_s - \partial_x z|_s \partial_z \rho|_z)\, dz, \tag{A.1}$$

where the vertical bars indicate whether the derivative is taken along an s- or a z-surface. Both terms on the right-hand side of Eq. (A.1) may have numerical values that are larger than the pressure gradient itself, therefore a small relative error in the terms on the right-hand side may lead to a large relative error on the left-hand side of Eq. (A.1). For instance in the case of no horizontal density gradients, the difference on the right-hand side of Eq. (A.1) is generally non-zero in a terrain following model. It is thus challenging to calculate the horizontal pressure gradient accurately when a terrain following vertical coordinate is used. The slope of the s-surface and the vertical density gradient must be taken into account. In a sill fjord the sill itself might create a pycnocline. This makes it especially challenging to calculate the horizontal pressure gradient since high vertical density gradients are present over the sill where the slope of the s-surface is typically large.

To minimize the PGE we compare two experiments PGE1 and PGE2 (cf. Table 1), one using the canonical transform that comes with ROMS (Shchepetkin and McWilliams, 2005) (PGE1) and the second, like MAIN, using a new transform and stretching (PGE2) as explained in the next paragraph. In contrast to MAIN we apply absolutely no forcing at the southern open boundary by setting the tidal amplitude to zero there. Moreover we replace the observed stratification with the "strong" stratification displayed in Fig. 8 to enhance the PGE
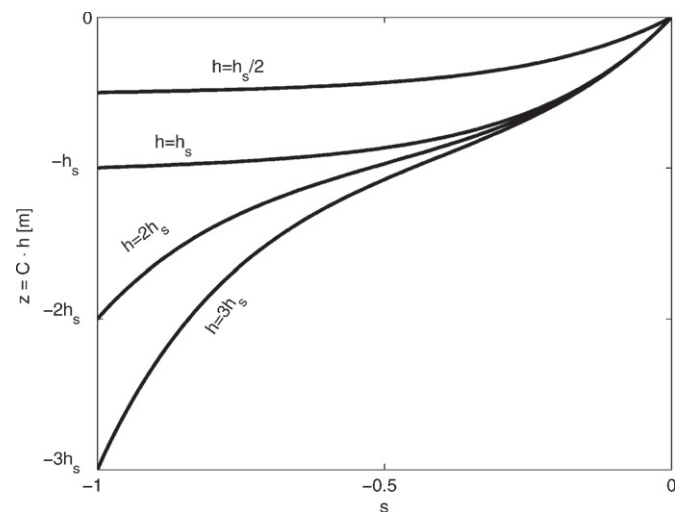

Fig. A1. The depth (in the case when $\zeta = 0$) as a function of s for four different water depths. The stretching function is calculated using Eq. (A.6) with $\theta_s = \theta_B = 4$. Note that $\partial_z s$ for all curves has its lowest value at $z = -h_s$, indicating high vertical resolution, except when the water depth is shallower than h_s.

error. We note that since the fluid is initially at rest, and no forcing is applied, any motion that develops is an artifact and due to the PGE.

To construct the new transform and stretching we basically make changes to two functions in the canonical version of ROMS. The first is a stretching function $C = f_s$ used to enhance the vertical resolution in certain parts of the water column. Several stretching functions are available (Mason et al., 2010; Shchepetkin and McWilliams, 2005; Song and Haidvogel, 1994). The second operation is to define the transformation function between the geopotential depth z and the s-surface. It takes the form

$$z = f_T (H, \zeta, C, h_c) \tag{A.2}$$

where H is the total water depth, ζ is the sea level elevation, C is the stretching function and h_c is a parameter called the critical depth. The transformation Eq. (A.2) then determines where in the vertical space the s-surface is located.

The parameter h_c is used to modify the coordinate above a certain critical depth. Two different transformations are available in ROMS. They differ in how h_c is incorporated in Eq. (A.2). If the critical depth is set to zero both transforms reduce to

$$z = C(s)(H + \zeta) + \zeta. \tag{A.3}$$

As is obvious the choice made for the transform and stretching function has an impact on the PGE. Consequently, by carefully choosing the transform and stretching functions, it is possible to minimize the strength of the PGE. By constructing a stretching function f_s that enhances the vertical resolution in the pycnocline, the relative error in the calculation of the vertical density gradient will be reduced. It is not possible to enhance the resolution in a

fixed depth (at the expense of the resolution above and below this depth) without also reducing the slope of the s-surface in this depth. Since the vertical gradient of the density generally is larger than the horizontal gradient, both terms on the RHS of Eq. (A.1) will be reduced.

To achieve this we introduce a dependence of the water depth in the stretching function C. In fact the weighted sum of two stretching functions is used, one that enhance the resolution near the bottom C_B and another that enhance the resolution near the surface C_s.

$$C(s, H) = (1 - \mu)C_B(s) + \mu C_s(s) \tag{A.4}$$

The bottom stretching function is written

$$C_B(s) = \frac{\sinh \theta_B(s+)}{\sinh \theta_B} - 1 \tag{A.5}$$

where θ_B is the bottom stretching parameter. The surface stretching function is written

$$C_s(s) = \frac{1 - \cosh \theta_B s}{\cosh \theta_s - 1} \tag{A.6}$$

where θ_s is the surface stretching parameter. The weight μ is

$$\mu = \frac{H - h_s}{H} \quad \text{if} \quad H > h_s, \tag{A.7}$$

where h_s is the depth of enhanced resolution. If $H < h_s$, then $\mu = 0$ and the stretching function is set to $C = C_B$. Fig. A1 illustrates how the resolution is enhanced in the depth near h_s for different water depths.
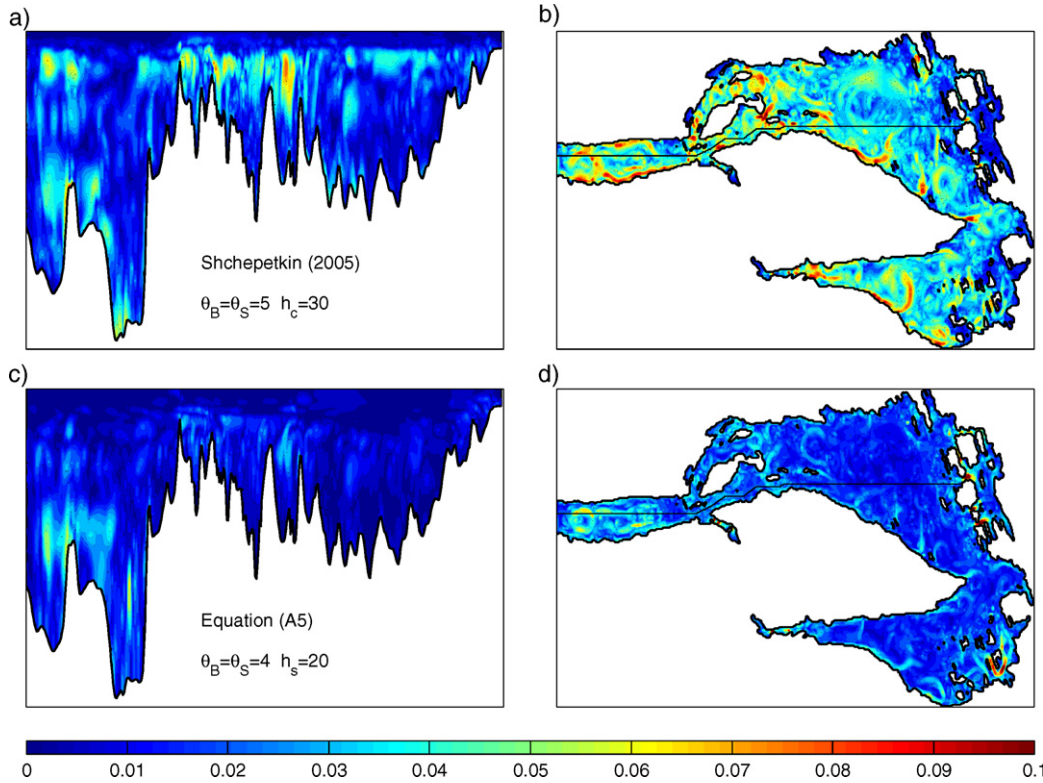

Fig. A2. The maximum currents caused by the pressure gradient error in the PGE1 (panels a and b) and PGE2 (panels c and d) experiments after after 3 days of simulation. The left-hand panels show the distribution of the maximum PGE currents along the section outlined by the black line in the right-hand panels, while the right-hand panels show their horizontal distributions regardless of depth. Current speed is indicated by color bar in m s^{-1}. Note the substantial reduction in PGE achieved in PGE2 compared to PGE1 almost everywhere except in a few hot spots.

Fig. A2 shows the results of the PGE1 and PGE2 experiments after 3 days (72 h). As is evident that the PGEs of PGE1 are substantial, in particular in the upper water masses including the pycnocline layer, and generate artificial currents as high as 0.1 m s^{-1}. Moreover most of the maximum currents are located at the levels where the propagating tidally induced, internal waves are present. Applying the new transform (PGE2) dramatically reduces the PGEs at or above sill level where it is needed most. We emphasize though that it does not reduce the PGEs to acceptable levels everywhere. In relatively deep waters outside of the Drøbak Sill (Station H1), the PGEs are still significant. Also in the inner Oslo Harbor there are significant PGEs. However, since the first one is located in the deep water outside of the sill and the second area is limited to the Oslo Harbor, we do not expect the artificial currents due to PGE to have any serious impact on our results. Consequently we have used the new transform in all the remaining experiments except VAL2.

We emphasize that although the new transform reduces the PGEs it may potentially give problems in deep waters where the vertical resolution becomes coarser when employing the new transform. As an example the bottom layers are as thick as 29 m if the water depth is 258 m when using the new transform. Nevertheless, at the levels where it matters the PGEs are reduced to acceptable levels.

References

Alford, M.H., 2003. Energy available for ocean mixing redistributed by long-range propagation of internal waves. Nature 423, 159–162. http://dx.doi.org/10.1038/nature01628.

Baalsrud, K., Magnusson, J., for vann-og avløpsteknisk samarbeid i indre Oslofjord, Fagrådet, 2002. Indre Oslofjord: natur og miljø. Fagrådet for vann- og avløpsteknisk samarbeid i indre Oslofjord http://books.google.no/books?id=SCZAMwEACAAJ.

Baines, P.G., 1982. On internal tide generation models. Deep Sea Res. A Oceanogr. Res. Pap. 29 (3), 307–338. http://dx.doi.org/10.1016/0198-0149(82)90098-X.

Bell, T.H., 1975. Topographically generated internal waves in the open ocean. J. Geophys. Res. 80 (3), 320–327. http://dx.doi.org/10.1029/JC080i003p00320.

Berge, J.A., Amundsen, R., Bjerkeng, B., Bjerknes, E., Espeland, S.H., Gitmark, J.K., Holth, T.F., Hylland, K., Imrik, C., Johnsen, T., Lømsland, E.R., Magnusson, J., Nilsson, H.C., Rohrlack, T., Sørensen, K., Walday, M., 2010. Monitoring of the pollution status of the Inner Oslofjord 2009 [in Norwegian]. Tech. Rep. NIVA report No. 5985. Norwegian Institute of Water Research (NIVA), Oslo, Norway.

Berntsen, J., Thiem, Ø., 2007. Estimating the internal pressure gradient errors in a sigma-coordinate ocean model for the Nordic Seas. Ocean Dyn. 57, 417–429. http://dx.doi.org/10.1007/s10236-007-0118-1.

Berntsen, J., Jarle, Xing, Jiuxing, Davies, Alan.M., 2008. Numerical studies of internal waves at a sill: sensitivity to horizontal grid size and subgrid scale closure. Cont. Shelf Res. 28 (1011), 1376–1393. http://dx.doi.org/10.1016/j.csr.2008.03.029.

Berntsen, J., Xing, J., Davies, A.M., 2009. Numerical studies of flow over a sill: sensitivity of the non-hydrostatic effects to the grid size. Ocean Dyn. 59, 1043–1059. http://dx.doi.org/10.1007/s10236-009-0227-0.

Beyer, F., Føyn, E., 1951. Hypoxia in the Oslofjord [in Norwegian]. Naturen 75, 289–306.

Bjerkeng, B., Göranson, C.G., Magnusson, J., 1978. Investigations of different alternatives for waste water disposal from sentralanlegg vest [in Norwegian]. Tech. Rep. NIVA report No. OR-1053. Norwegian Institute of Water Research (NIVA), Oslo, Norway.

Carter, G.S., Merrifield, M.A., Becker, J.M., Katsumata, K., Gregg, M.C., Luther, D.S., Levine, M.D., Boyd, T.J., Firing, Y.L., 2008. Energetics of M$_2$ barotropic-to-baroclinic tidal conversion at the Hawaiian Islands. J. Phys. Oceanogr. 38, 2205–2223.

Dolven, J.K., Alve, E., Rygg, B., Magnusson, J., 2013. Defining past ecological status and in situ reference conditions using benthic foraminifera: a case study from the Oslofjord, Norway. Ecol. Indic. 29, 219–233. http://dx.doi.org/10.1016/j.ecolind.2012.12.031.

Egbert, G.D., Ray, R.D., 2000. Significant dissipation of tidal energy in the deep ocean inferred from satellite altimeter data. Nature 405, 775–778. http://dx.doi.org/10.1038/35015531.

Gade, H.G., 1967. The Oslofjord and its pollution problems, investigations 1962–1965. Tech. Rep. Report OR-0191c. Norwegian Institute of Water Research (NIVA), Oslo, Norway.

Gade, H.G., 1970. Hydrographic investigations in the Oslofjord, a study of water circulation and exchange processes. Tech. Rep. Rep 24, Geophys. Inst., Div. A. University of Bergen, Norway.

Gill, A.E., 1982. Atmosphere-ocean dynamics. International Geophysical Ser. 30. Academic Press vol

Gregg, M.C., 1987. Diapycnal mixing in the thermocline: a review. J. Geophys. Res. 92 (C5), 5249–5286.

Haidvogel, D.B., Arango, H., Budgell, P.W., Cornuelle, B.D., Curchitser, E., Lorenzo, E.D., Fennel, K., Geyer, W.R., Hermann, A.J., Lanerolle, L., Levin, J., McWilliams, J.C., Miller, A.J., Moore, A.M., Powell, T.M., Shchepetkin, A.F., Sherwood, C.R., Signell, R.P., Warner, J.C., Wilkin, J., 2008. Ocean forecasting in terrain-following coordinates: formulation and skill assessment of the regional ocean modeling system. J. Comput. Phys. 227 (7), 3595–3624. http://dx.doi.org/10.1016/j.jcp.2007.06.016.

Haney, R.L., 1991. On the pressure gradient force over steep topography in sigma coordinate ocean models. J. Phys. Oceanogr. 21 (4), 610–619.

Inall, M.E., 2009. Internal wave induced dispersion and mixing on a sloping boundary. Geophys. Res. Lett. 36, L05604 http://dx.doi.org/10.1029/2008GL036849.

Jayne, S.R., Laurent, L.C.S., 2001. Parameterizing tidal dissipation over rough topography. Geophys. Res. Lett. 28, 811–814. http://dx.doi.org/10.1029/2000GL012044. http://dx.doi.org/10.1029/2000GL012044.

Kang, D.V., Fringer, O., 2012. Energetics of barotropic and baroclinic tides in the monterey bay area. J. Phys. Oceanogr. 42, 272–290.

Ledwell, J.R., Montgomery, E.T., Polzin, K.L., Laurent, L.C.S., Schmitt, R.W., Toole, J.M., 2000. Evidence of enhanced mixing over rough topography in the abyssal ocean. Nature 403, 179–182. http://dx.doi.org/10.1038/35003164.

Lepland, A., Bøe, R., Lepland, A., Totland, O., 2009. Monitoring the volume and lateral spread of disposed sediments by acoustic methods, Oslo Harbor, Norway. J. Environ. Manag. 90 (11), 3589–3598. http://dx.doi.org/10.1016/j.jenvman.2009.06.013.

Mason, E., Molemaker, J., Shchepetkin, A.F., Colas, F., McWilliams, J.C., Sangrà, P., 2010. Procedures for offline grid nesting in regional ocean models. Ocean Model. 35 (1-2), 1–15. http://dx.doi.org/10.1016/j.ocemod.2010.05.007.

Nash, J.D., Alford, M.H., Kunze, E., 2005. Estimating internal wave energy fluxes in the ocean. J. Atmos. Ocean. Technol. 22 (10), 1551–1570. http://dx.doi.org/10.1175/JTECH1784.1.

Osborn, T.R., 1980. Estimates of the local rate of vertical diffusion from dissipation measurements. J. Phys. Oceanogr. 10, 8389

Peters, H., Bokhorst, R., 2001. Microstructure observations of turbulent mixing in a partially mixed estuary. Part II: salt flux and stress. J. Phys. Oceanogr. 31 (4), 1105–1119.

Shchepetkin, A.F., McWilliams, J.C., 2003. A method for computing horizontal pressure-gradient force in an oceanic model with a nonaligned vertical coordinate. J. Geophys. Res. 108, 1–34. http://dx.doi.org/10.1029/2001JC001047.

Shchepetkin, A.F., McWilliams, J.C., 2005. The regional ocean modeling system (ROMS): a split-explicit, free-surface, topography-following coordinate ocean model. Ocean Model. 9, 347–404.

Shchepetkin, A.F., McWilliams, J.C., 2009. Correction and commentary for ocean forecasting in terrain-following coordinates: formulation and skill assessment of the regional ocean modeling system by Haidvogel et al., J. Comp. Phys. 227, pp. 3595-3624. J. Comp. Phys. 228 (24), 8985–9000. http://dx.doi.org/10.1016/j.jcp.2009.09.002.

Sjöberg, B., Stigebrandt, A., 1992. Computations of the geographical distribution of the energy flux to mixing processes via internal tides and the associated vertical circulation in the ocean. Deep Sea Res. A Oceanogr. Res. Pap. 39 (2), 269–291. http://dx.doi.org/10.1016/0198-0149(92)90109-7.

Song, T., Haidvogel, D., 1994. A semi-implicit ocean circulation model using a generalized topography-following coordinate system. J. Comput. Phys. 115, 228–244.

St. Laurent, L., Garrett, C., 2002. The role of internal tides in mixing the deep ocean. J. Phys. Oceanogr. 32, 2882–2899.

Staalstrøm, A., Aas, E., Liljebladh, B., 2012. Propagation and dissipation of internal tides in the Oslofjord. Ocean Sci. 8, 525–543.

Staalstrøm, Andre, Arneborg, Lars, Liljebladh, Bengt, Broström, Göran, 2015. Observations of turbulence caused by a combination of tides and mean baroclinic flow over a fjord sill. J. Phys. Oceanogr. 45 (2), 355–368.

Stigebrandt, A., 1976. Vertical diffusion driven by internal waves in a sill fjord. J. Phys. Oceanogr. 6, 486–495.

Stigebrandt, A., 1979. Observational evidence for vertical diffusion driven by internal waves of tidal origin in the Oslofjord. J. Phys. Oceanogr. 9, 435–441.

Umlauf, L., Burchard, H., 2003. A generic length-scale equation for geophysical turbulence models. J. Mar. Res. 61, 235–265.

Warner, J.C., Sherwood, C.R., Arango, H.G., Signell, R.P., 2005. Performance of four turbulence closure methods implemented using a generic length scale method. Ocean Model. 8, 81–113.

Wunsch, C., Ferrari, R., 2004. Vertical mixing, energy, and the general circulation of the oceans. Annu. Rev. Fluid Mech. 36, 281–314. http://dx.doi.org/10.1146/annurev.fluid.36.050802.122121.

Xing, J., Davies, A.M., 2007. On the importance of non-hydrostatic processes in determining tidally induced mixing in sill regions. Cont. Shelf Res. 27, 2162–2185. http://dx.doi.org/10.1016/j.csr.2007.05.012.

Xing, J., Davies, A.M., 2011. On the interaction of internal tides over two adjacent sills in a fjord. J. Geophys. Res. 116, 1–34. http://dx.doi.org/10.1029/2010JC006333.